

Materials Research Letters

ISSN: 2166-3831 (Online) Journal homepage: www.tandfonline.com/journals/tmrl20

Recent progress in synthesis of MAX phases and oxidation & corrosion mechanism: a review

Min Guo, Guoqin Cao, Haoyu Pan, Junhong Guo, Chaoyang Chen, Baofeng Zhang & Junhua Hu

To cite this article: Min Guo, Guoqin Cao, Haoyu Pan, Junhong Guo, Chaoyang Chen, Baofeng Zhang & Junhua Hu (2024) Recent progress in synthesis of MAX phases and oxidation & corrosion mechanism: a review, Materials Research Letters, 12:11, 765-796, DOI: 10.1080/21663831.2024.2379567

To link to this article: https://doi.org/10.1080/21663831.2024.2379567

© 2024 The Author(s). Published by Informa UK Limited, trading as Taylor & Francis Group.

Published online: 11 Aug 2024.

Submit your article to this journal

Article views: 6546

View related articles

View Crossmark data

Citing articles: 52 View citing articles

Full Terms & Conditions of access and use can be found at
https://www.tandfonline.com/action/journalInformation?journalCode=tmrl20

MATER. RES. LETT.
2024, VOL. 12, NO. 11, 765–796
https://doi.org/10.1080/21663831.2024.2379567

MATERIALS RESEARCH LETTERS
Taylor & Francis
Taylor & Francis Group

REVIEW ARTICLE

OPEN ACCESS Check for updates

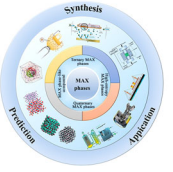
Recent progress in synthesis of MAX phases and oxidation & corrosion mechanism: a review

Min Guo[a,b], Guoqin Cao[a,b,c], Haoyu Pan[a,b], Junhong Guo[a,b], Chaoyang Chen[a,b], Baofeng Zhang[d] and Junhua Hu[a,b,c]

[a]School of Materials Science and Engineering, Zhengzhou University, Zhengzhou, People's Republic of China; [b]State Centre for International Cooperation on Designer Low-carbon & Environmental Materials, Zhengzhou University, Zhengzhou, People's Republic of China; [c]Zhongyuan Critical Metals Laboratory, Zhengzhou University, Zhengzhou, People's Republic of China; [d]Faculty of Engineering, Huanghe Science and Technology College, Zhengzhou, People's Republic of China

ABSTRACT

Layered MAX phases possess distinctive chemical, physical, electrical, and mechanical properties due to their amalgamation of metallic and ceramic characteristics. Understanding the corrosion mechanisms of MAX phases in various extreme environments is crucial. This paper commenced by scrutinizing synthesis techniques for MAX phase powders, thin films, and bulk materials, with a focus on fabrication processes and formation mechanisms. Subsequently, it delved into corrosion & oxidation mechanisms in diverse environments, emphasized their unique self-healing properties, and outlined future research directions. This comprehensive and systematic review aims to furnish researchers with effective guidance for selecting MAX phases based on different application environments.



ARTICLE HISTORY
Received 26 April 2024
Accepted 27 June 2024

KEYWORDS
MAX phases; synthesis; oxidation; corrosion; mechanism

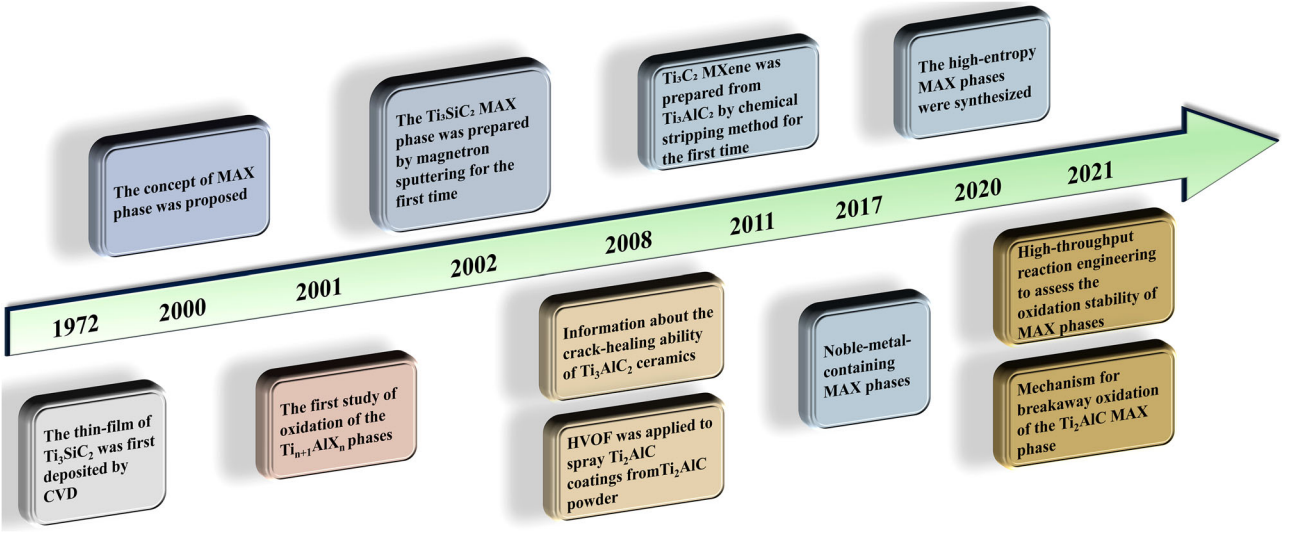
1. Introduction

The MAX phases were first discovered in the late 1970s by Novotny et al with the name of 'H-phase materials' which is a class of nano-layered carbides and nitrides. The general formula is $M_{n+1}AX_n$, where n equals $1 \sim 6$, M belongs to an early transition metal, A is an A-group (mostly I IIA and IVA) element, and X can be C, B or N [1–4]. The crystal structure of the MAX phases is characterized by different $M_{n+1}X_n$ layers and A layers alternately stacked along the c-axis. Based on the value of 'n', traditional MAX phases were categorized into three groups: 211 phases (Ti_2AlC), 312 phases (Ti_3AlC_2) and 413 phases (Nb_4AlC_3) [5–7]. Recently, MAX phases with higher values of 'n' have also been discovered, including 514 phases ($(Ti_{0.5}Nb_{0.5})_5AlC_4$) [8], 615 phases ($Ta_6AlC_5$) [9], 716 phases ($Ti_7SnC_6$) [10]. Additionally, by doping elements in the M, A, or X site, new MAX phases can be synthesized, such as $(Ti_{0.5}Zr_{0.5})_2AlC$ [11], $Ti_3(Al_{1-x}Si_x)C_2$ [12], $Ti_2Al(C_x,N_{1-x})_y$ [13] etc. In addition to the traditional MAX phase structures, there are also hybrid structures. Notable examples include the 725 phases ($Ti_7Si_2C_5$) [14] and the 523 phases ($Ti_5Al_2C_3$) [15]. The 725 and 523 phases are intergrown phases with alternating layers of 211 and 312 (or 312 and 413).

The MAX phases were typically fabricated using methods such as hot press sintering (HP) [16], spark plasma sintering (SPS) [17], mechanical alloying (MA) [18], self-propagating high-temperature synthesis (SHS) [19], physical vapor deposition (PVD) [20] and chemical vapor deposition (CVD) [21]. In the preparation process, a primary challenge arised from the formation of intermediate phases, leading to a reduction in purity. Recently,

CONTACT Guoqin Cao caoguoqin@zzu.edu.cn; Junhua Hu hujh@zzu.edu.cn School of Materials Science and Engineering, Zhengzhou University, Zhengzhou 450001, People's Republic of China; State Centre for International Cooperation on Designer Low-carbon & Environmental Materials, Zhengzhou University, 100# Kexue Avenue, Zhengzhou 450001, People's Republic of China; Zhongyuan Critical Metals Laboratory, Zhengzhou University, Zhengzhou, People's Republic of China

© 2024 The Author(s). Published by Informa UK Limited, trading as Taylor & Francis Group.
This is an Open Access article distributed under the terms of the Creative Commons Attribution License (http://creativecommons.org/licenses/by/4.0/), which permits unrestricted use, distribution, and reproduction in any medium, provided the original work is properly cited. The terms on which this article has been published allow the posting of the Accepted Manuscript in a repository by the author(s) or with their consent.



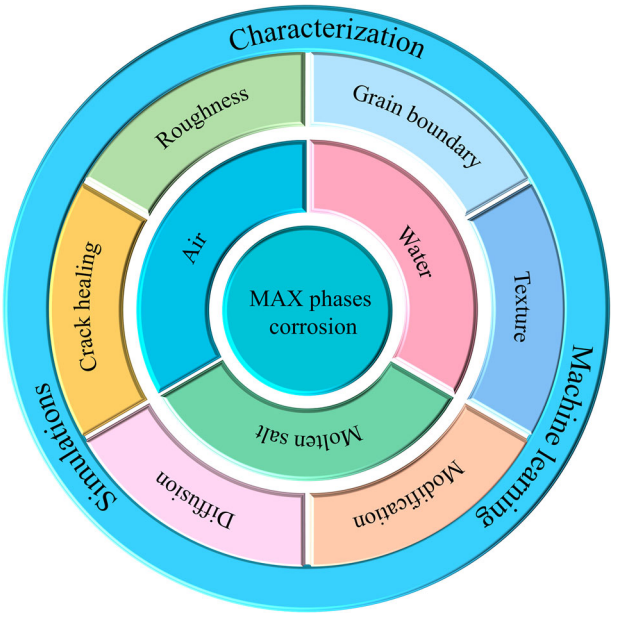
Scheme 1. A brief history for the development of MAX phases.

the formation mechanism and theoretical research of MAX phases have received extensive attention [3,4,22].

The MAX phases exhibit unique properties arising from the mixed covalent-ionic-metallic nature of their chemical bonds and the special nanolayered structure. These properties combine characteristics of ceramics and metals, including good ductility, high thermal and electrical conductivity, superior oxidation resistance, remarkable high-temperature stability, and excellent radiation resistance. Such distinctive features make MAX phases as an ideal material family for various applications, including thermal shock-resistant refractories, electrical contact coatings, neutron radiation-resistant materials, etc [23,24]. In additon, MAX phase is the precursor of MXene. The MXene can be formed by etching the A-position atoms of MAX phase. Due to its advantages of high conductivity, hydrophilicity, large surface area, it has a wide range of applications in catalysis and energy storage [25]. Researchers have extensively studied these unique properties of the MAX phases since the early 2000s [1,21,22,26–35], as illustrated in Scheme 1.

The most significant application of MAX is high-temperature materials due to its superior oxidation resistance in various environments, including atmospheric conditions, high-temperature water environments, critical water conditions, and molten corrosive media. This application primarily relies on its unique layered nanostructures and characteristic elements. Over the past two decades, considerable attention has been devoted to MAX phases such as Cr_2AlC [36], Ti_2AlC [37] and Ti_3AlC_2 [38] which showed excellent antioxidant properties in harsh environment. Corrosion or oxidation resistance hinges on the formation of a dense protective layer on the surface and a good thermal match between the protective layer and the substrate. Ti_2AlC exhibits almost the same coefficient of thermal expansion (CTE) (7.4×10^{-6} /K from 25°C to 1300°C) with in-situ formed Al_2O_3(7.9×10^{-6} /K from 25°C to 1000°C and 9.0×10^{-6} from 25°C to 1500°C, respectively) [37]. Consequently, thermoelastic stress is minimized (the residual thermal stress on Al_2O_3 can be reduced to 7 times compared to nickel superalloys), reducing and preventing premature spalling. The MAX phases with Al element were inherently self-healing under oxidation conditions [39–42]. Due to the relatively weak M-A bond, A atoms tend to diffuse outward from the A layer and are more easily oxidized when exposed to an oxygen environment at high temperatures. Therefore, existing microcracks can be filled by the formation of A-oxides.

The intricate corrosion environment has presented challenges to the application of MAX. For instance, in high-temperature oxidation environments with water or vapor, hydroxide ions selectively bond with Si and Al in the A-site of MAX phases, hindering the formation of dense passivation structures. Achieving matching oxidation resistance under both air and water vapor environments requires a theoretical understanding of the formation and destruction mechanisms of the oxide layer. The formation of the protective layer is influenced by the diffusion of elements. Various forms of element diffusion in MAX phases, particularly in coating MAX phases, have not been thoroughly investigated. The microscale diffusion mechanisms of elements in different environments remain unclear. To predict and control the behavior of MAX phases at different temperatures, it is essential to systematically study the phase formation processes, microstructure evolution, and oxidation behavior in various environments.



Scheme 2. A review of different application environments and corrosion resistance factors of MAX phases.

This review aims to summarize the oxidation behavior and mechanisms of MAX phases in various environments. This endeavor contributes to a better understanding of the application of MAX phases in diverse settings, along with existing challenges and potential solutions. The review briefly outlines preparation methods for various MAX phases and summarizes their formation mechanisms. Furthermore, it explores MAX phase oxidation mechanisms in different environments, with a focus on factors like composition, surface texture, oxide structure, and the destruction mechanism, as depicted in Scheme 2.

The review also addresses the multi-component oxidation behavior and mechanisms of MAX phases. Furthermore, a brief discussion on the impact of molten salt on MAX phase corrosion enhances our understanding of MAX phase material behavior in fourth-generation reactor environments. Finally, the review succinctly summarizes the main research achievements and outlines future research directions for MAX phases in diverse corrosion fields.

2. Preparation of MAX phases

MAX phases were produced in various forms, including bulk material [34], thin layer films [43] or thick coatings [44], and powders [45]. Bulk MAX phases blocks were commonly utilized for structural materials, such as turbine blades [46]. Thin films were typically deposited by Magnetron sputtering (Figure 1(a)). Thick coatings were fabricated by thermal spraying (including laser cladding (Figure 1(b)), plasma spraying (Figure 1(c)) and high-speed oxygen fuel (HVOF) spraying) and cold spraying technology, which were used in various industries such as aerospace, nuclear power plants, ships and oceans [47,48].

Different forms of materials underwent distinct changes during preparation and phase transition, necessitating specific conditions. For instance, powder preparation requires addressing issues related to excessive specific surface area and surface overexposure. The film preparation process primarily involved the nucleation of atoms islands on the substrate, requiring careful consideration of two-dimensional atom diffusion. In the early stages, research focused mainly on Si-containing MAX phases such as Ti_3SiC_2. In recent years, an increasing number of studies have emerged on Al-containing MAX phases, such as Ti_2AlC, Cr_2AlC, etc [20,35,49,50]. Higher-order MAX phase structures were also reported to form at higher temperatures due to longer diffusion lengths [1]. In this section, the preparation methods and formation mechanism of different forms of MAX phases were briefly discussed.

2.1. Preparation of MAX phase powers

The synthesis of MAX powders has been reported using various methods, such as pressureless sintering [53], mechanical alloying [54], self-propagation high temperature synthesis [55], molten salt synthesis(MSS) [56]. Su et al. [57] synthesized high purity (98.7wt %) Ti_3SiC_2 powder using coir carbon, Ti and Si as raw materials in a flowing argon atmosphere of 1673 K through a simple press-free sintering process. The reactions can be described by the following equations.

$$Ti(s) + C(s) \rightarrow TiC(s) \quad (1)$$

$$5Ti(s) + 3Si(s,l) \rightarrow Ti_5Si_3(s) \quad (2)$$

$$Ti_5Si_3(s) + 4TiC(s) + 2C(s) \rightarrow 3Ti_3SiC_2(s) \quad (3)$$

Etebarian et al. [56] synthesized Ti_3SiC_2 phase powder using the molten salt synthesis (MSS) method with relatively high purity (93%) at 1200°C for 2 h. In the MSS method, low melting salt(s) such as NaCl or a combination of NaCl and KCl were used as the reaction medium to accelerate the reaction process. The solubility of reactants in the salt medium provides a quite homogeneous mixture, and the final products were formed in the molten salt medium at lower temperatures and shorter. The synthesis process was determined by the relative dissolution rate of the reactants in the molten salt.

For powder sintering to produce MAX phases, temperatures exceeding 1300°C led to significant Al evaporation, causing lattice distortion and reduced fracture

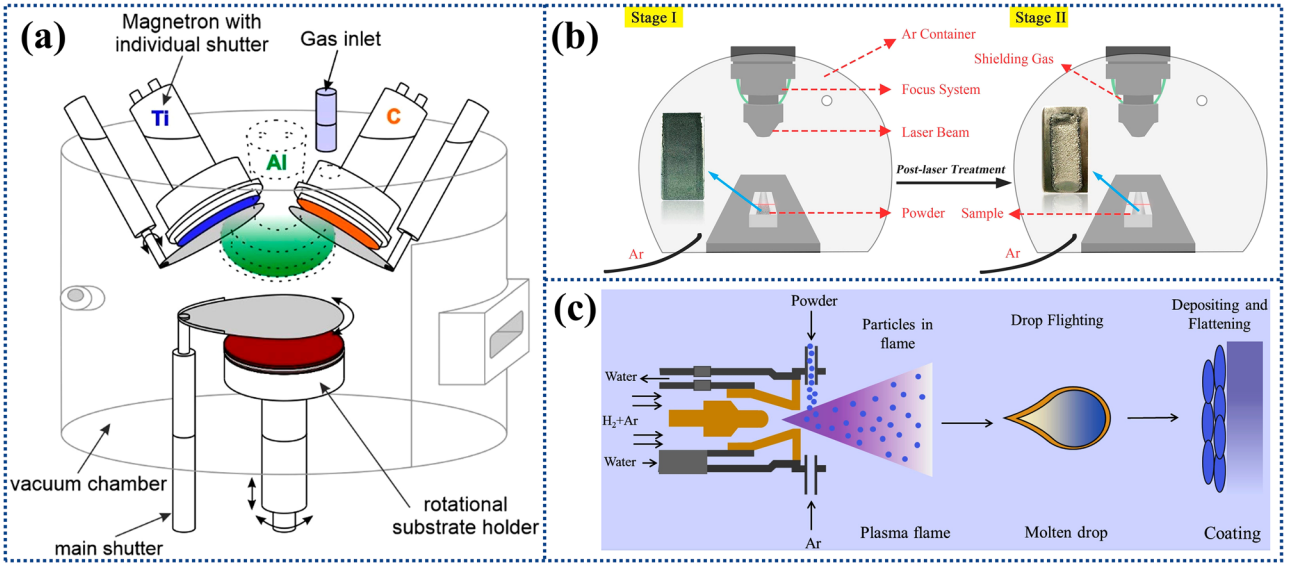


Figure 1. Schematic illustration of MAX coating preparation (a) magnetron sputtering process (reprinted with permission from [20]), (b) laser cladding process (reprinted with permission from [51]), (c) plasma spraying process (reprinted with permission from [52]).

toughness within the MAX phase. To enhance the purity of synthesized MAX phases, higher A-element content in the initial material was required to compensate for evaporative losses during high-temperature synthesis. Otherwise, residual M_xX_y phases or MAX phases with higher 'n' values may remain in the final product. However, excessively high A-element content in the starting materials might result in residual M_xA_y compounds. When using pure metal powder sintering for MAX phase synthesis, the formation temperature usually exceeded 1100°C. Fortunately, MAX phases can be obtained at low temperature by introducing intermediate phase MX compounds into the raw materials.

2.2. Preparation of MAX phase coatings

The preparation of MAX coatings mainly involves PVD, CVD, laser cladding and plasma spraying. Thermal spraying technology was commonly used in thick coating fabrications process [47,58]. The source material, which can be a powder or wire, is heated or even melted by thermal energy through chemical (combustion flame) or electrical (plasma or laser) methods, and then sprayed onto the substrate at a high speed. However, the MAX phase composite coating is unstable at high temperature when sprayed with high energy. The high energy beam could promote the decomposition of in-situ synthesized MAX phase. Proper heat treatment of the coating after laser cladding was required to enhance the interatomic diffusion in the coating, reduce the residual stress, and improve the microstructure of the coating [51].

The PVD process mainly includes direct current magnetron sputtering (DCMS), arc ion plating (AIP) and radio frequency magnetron sputtering (RFMS). There are mainly three synthesis ways for the preparation of MAX film, which are multi-target co-sputtering deposition [50], multi-target sequential deposition [20,59–61] and single-target sputtering deposition [49,62,63]. Heating the substrate during sputtering facilitates in-situ crystallization of the MAX phase. The non-in-situ annealing a bunch of amorphous or partially crystalline nanolayer has also been reported. During the sputtering process, the monolayer thickness, temperature & time have important effects on the evolution of MAX phase microstructure.

As described by Eklund et al. [3,4], the formation mechanism of MAX phase films focuses on the key role of sputtering and chemical vapor deposition (CVD) techniques. These methods allow for the precise control of film composition and morphology through careful selection of target materials, substrates, and deposition parameters. Post-deposition annealing processes are critical for enhancing crystallinity and phase purity. The choice of substrate and optimization of deposition conditions, such as temperature and pressure, significantly influence the quality and properties of the resulting MAX phase films. These processes enable the creation of high-quality thin films with tailored properties suitable for various applications.

Palmquist et al. [29] synthesized Ti_3SiC_2 MAX phase films using two approaches: Ti and Si sputtering targets combined with C60 evaporation and sputtering from a Ti_3SiC_2 composite target. The results demonstrated that both methods successfully produced single-crystal epitaxial Ti_3SiC_2 films at a growth temperature of 900°C. However, films deposited from the composite target at temperatures below 900°C showed no signs of the

Ti_3SiC_2 phase. In contrast, the C60 precursor method yielded crystallized Ti_3SiC_2 films at a lower temperature of 700°C, though the film quality was inferior.

The nano-layered coatings enabled shorter diffusion lengths. Additionally, the deposited multilayer material, being a high-energy substance, stored internal chemical energy that promoted the growth of MAX phases, thereby reducing their formation temperature. Recently, researchers employed a method of sequential atomic layer sputtering to fabricate uniformly thick M/A/X films [20,60,64]. The mechanisms of phase formation and the formation temperature were investigated.

Tang et al. [61] investigated the synthesis and characterization of Ti_2AlC coatings by sputtering a multilayer system consisting of Ti/Al/C monolayers (Figure 2(a1)). Annealing at 600°C resulted in the formation of a mixed intermetallic Al_3Ti and TiC. The crystalline transition from the competing non-MAX phases to Ti_2AlC MAX phase occurred in the region of 600–700°C. Pure phase of Ti_2AlC coating was obtained after 800°C annealing for 10 min with an average grain size around 20 nm (Figure 2(a2)). The special arrangement of just 10 nm for the thickest layer (Ti), guaranteed a short diffusion length and higher surface activity. Due to the nanoscale effects, a successful synthesis of pure Ti_2AlC coating at relative low temperature was achieved. In addition, with the temperature rising to 900°C, the Ti_3AlC_2 MAX phase gradually crystallized (Figure 2(a3)), The reaction mechanism was shown in Figure 2(a4).

Nucleation and growth of MAX phase through PVD required a threshold temperature to allow the atoms to have sufficient mobility and energy. In addition to Ti_2AlC, the preparation of Cr_2AlC was also investigated. The diffusion of Cr and C in the MAX phase was more favorable kinetically, because the bond energy of Cr-C was lower than that of Ti-C. Thus, the synthesis temperature of Cr_2AlC was the lowest among 211 MAX carbides. In addition, the initial crystallization temperature of the specific MAX phase was closely related to the thermodynamic stability of the corresponding binary carbide. Before the highly ordered MAX phase structure were formed, the formation of intermediate binary carbides or solid solution phases were inevitable during annealing. The thermodynamic stability of binary chromium carbide was much lower than that of binary titanium carbide, so for the formation of Ti_2AlC, a higher energy barrier (i.e. a higher synthesis temperature was required) must be overcome. Zhang et al. [62] studied the microstructure evolution of amorphous Cr-Al-C coatings prepared by DC magnetron sputtering from a compound target. At annealing temperature below 500°C, the coating had an amorphous structure (Figure 2(b1)). With the increase of annealing temperature, the coating was composed of $(Cr,Al)_2C_x$ solid solution, amorphous structure and Cr_2AlC MAX phase at 570°C (Figure 2(b2)). Cr_2AlC MAX phase was basically formed except for a small amount of incomplete solid solution at 700°C. With a further increase of temperature, the crystalline Cr_2AlC MAX phase remained basically stable at 800°C (Figure 2(b3)).

Multiple components require higher temperatures, For example, Azina et al. [49] studied the synthesis of MAX films from a $(Ti,Zr)_2AlC$ compound target. At first, due to preferential sputtering or the abundance of carbides on the target surface, only carbides were generated. High substrate temperatures and longer deposition times result in films primarily composed of (Ti, Zr)C carbides, The temperature must exceed 900°C to form MAX phases. Therefore, these carbides are considered as an intermediate layer that promoted the nucleation of MAX phases. The growth mechanism started with the formation of mixed (Ti, Zr)C carbides, followed by the nucleation and growth of aluminides, ultimately leading to the solid-state diffusion of Al into the carbides, forming the MAX phase at a temperature above 900°C.

The high post-annealing temperature ($>$ 700°C) limited MAX phase (Ti_2AlC) application, especially for the coating application. Abdulkadhim et al. [65] prepared TiC_x/Al bilayer films by combined magnetron sputtering and deduced that when $x < 0.7$, Upon annealing, TiC_x reacts with Al to form Ti–Al-based intermetallic. At temperatures as low as 700°C, Al inserted into TiC_x directly formed the MAX phase.

Wang et al. [50] designed and prepared $TiC_{0.65}$/Al multilayer films (Figure 2(c1)). By extending the annealing time, they successfully synthesized the Ti_2AlC phase at 550°C/100 h (Figure 2(c2)), which was the lowest reported synthesis temperature in the literature so far (Figure 2(c3)). The Al diffusion-controlled intercalation process played the key factor to reduce the formation temperature of Ti_2AlC MAX phase.

In situ generation and detection technology is widely used in various fields such as energy storage and catalysis [66–70]. In-situ X-ray diffraction (XRD) enables characterization of the phase composition, microstructure, and residual strain state of the coating as a function of temperature [71,72]. Yuan et al. [71] employed in-situ X-ray diffraction to investigate the phase evolution of deposited M-Al-C (M = Ti, V, Cr) coatings concerning temperature variations. The results revealed that the Ti_2AlC exhibited the highest negative formation energy, with a Debye temperature of 732 K, surpassing V_2AlC at 696 K and Cr_2AlC at 644 K, making it the most resistant to formation. At 400°C, crystallization peaks for Cr_2C initially appeared at 42.7° with a (101) preferred orientation, yet Cr_2AlC phase formation did not occur. Furthermore, at

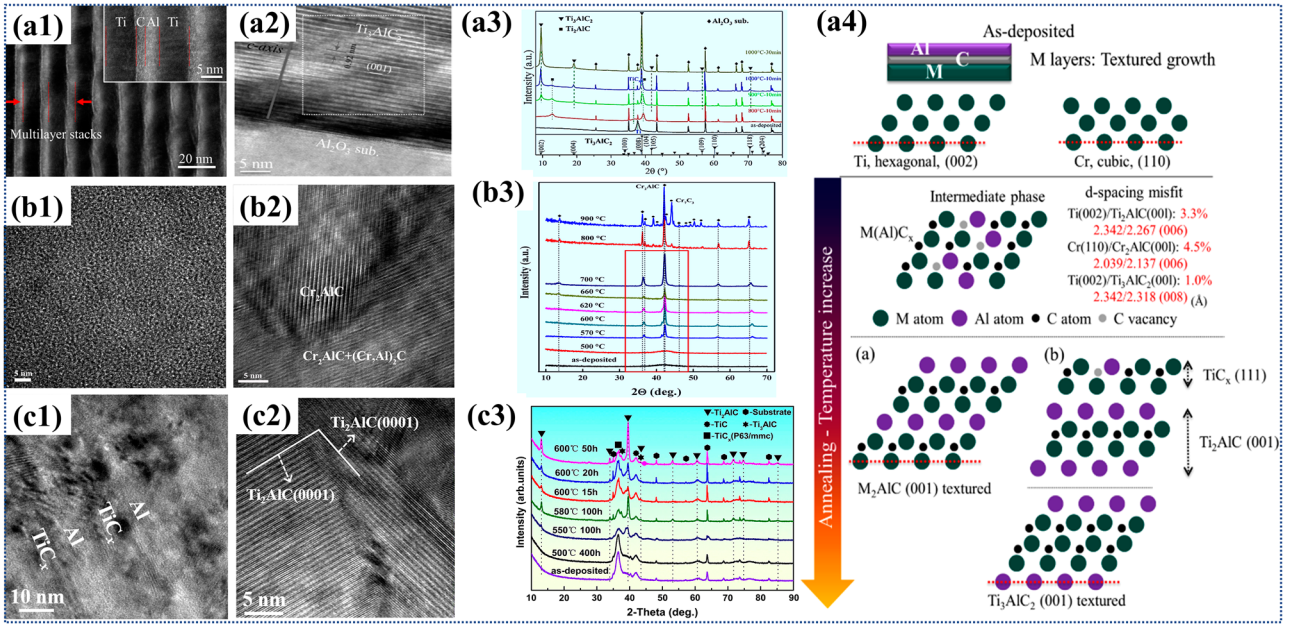


Figure 2. (a1) Low-magnification TEM images of as-deposited Ti-Al-C multilayer coating. (a2) Microstructures of Ti-Al-C coatings after 100 h of annealing at 550°C. (a3) XRD spectra of the as-deposited Ti-Al-C coatings and the annealed coatings at different annealing temperatures and time. (a4) Proposed schematic illustration of mechanisms for growth of basal plane textured MAX phase coatings via annealing of M/C/Al reactive multilayers (reprinted with permission from [60]) (b1) HRTEM image of the as-deposited Cr-Al-C coating. (b2) HRTEM image in local region. (b3) XRD patterns of the coatings annealed at 500–900°C for 1 h, as well as the as-deposited coating (reprinted with permission from [62]). (c1) Low-magnification TEM images of as-deposited Ti-Al-C multilayer coating, (c2) HRTEM images, (c3) XRD spectra of the as-deposited Ti-Al-C coatings and the annealed coatings at different annealing temperatures and time (reprinted with permission from [50]).

500°C, the peak at 42.7° shifted to a lower 2θ value, potentially due to the incorporation of Al into the hexagonal structure of Cr_2C. Upon further elevation of the temperature to 800°C, the intensity of the Cr_2AlC peak increased notably, especially the (103) crystal plane. These findings provided a theoretical basis for further understanding of the phase formation mechanism of MAX phase coatings.

In recent years, high power pulsed magnetron sputtering (HiPIMS) has received much attention due to its increased plasma density and ionization degree. These advantages enabled it to regulate the coating microstructure, enhance the migration and diffusion of surface bound atoms, and significantly improved the density, mechanical properties, and wear resistance of the coating [73,74].

Alamid et al. [73] firstly utilized high-power impulse magnetron sputtering (HIPIMS) technology to deposit Ti-Si–C films from a Ti_3SiC_2 composite target. The results indicated that the film composition, particularly the carbon content, depended on the substrate tilt angle and Ar pressure. When deposited at a substrate tilt angle of 90°, the Nowotny phase $Ti_5Si_3C_x$ was present in the films. Due to the high degree of ionization and the differences in ionization degrees among the three elements in the target, the composition of the deposited film differed from the nominal target composition, which could be controlled to some extent by appropriately selecting the process parameters. Under the same conditions, films deposited using direct current magnetron sputtering (DCMS) were rough and porous. Compared to DCMS, HIPIMS significantly improved the smoothness and density of the film quality.

Compared to DCMS, HiPIMS technology enhances the plasma ion concentration and kinetic energy, leading to the formation of inherent TiAlx nanocrystals within Ti-Al-C coatings instead of obtaining amorphous coatings [74]. TiAlx compounds typically was acted as intermediate products in the transformation from Ti-Al-C amorphous phase to Ti-based MAX phases. The inherent crystallinity of coatings deposited by HiPIMS undoubtedly contributed to this phase transition. Thus, the transformation of TiAlx compounds to MAX phases was more prone to occur than the mutual diffusion and reaction of Ti, Al, and C. In the end, HIPIMS facilitated the generation of Ti_3AlC_2 phase after low temperature annealing at 700°C.

2.3. Preparation of MAX phase bulks

Early bulk MAX phases were mainly prepared by the combination of spark plasma sintering (SPS) [58], with hot pressing (HP) [75] or hot isostatic pressing (HIP)

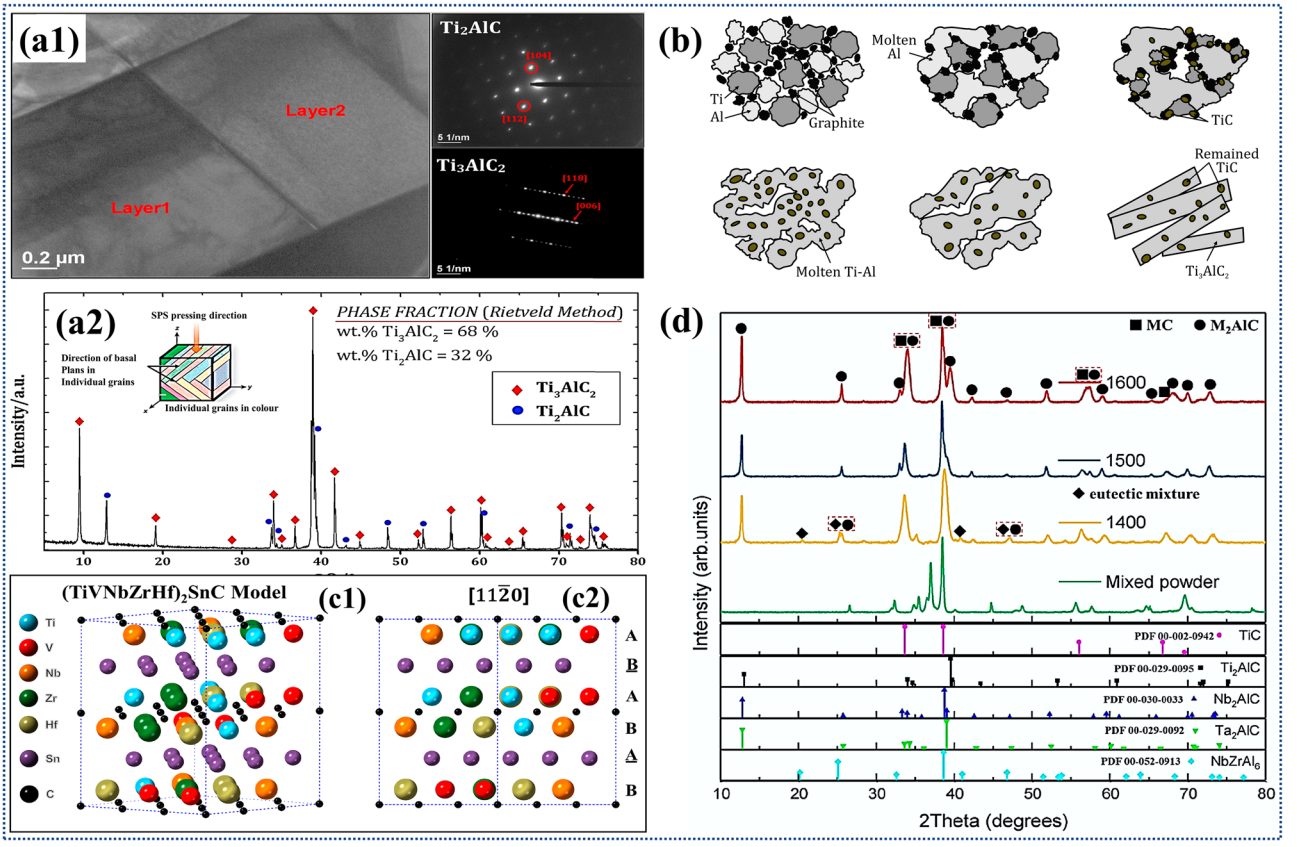


Figure 3. (a1) Abnormal grain growth (AGG) of Ti_3AlC_2 and Ti_2AlC grains in the Ti_3AlC_2—Ti_2AlC composite matrix. (a2) XRD patterns of the resulting bulk MAX phase composite obtained by in-situ SPS of elemental Ti, Al and C powder mixture (reprinted with permission from [78]) (b) Schematic illustration of formation mechanism of Ti_3AlC_2 MAX phase (reprinted with permission from [79]) (c1–c2) Schematic of the $(TiVNbZrHf)_2SnC$ supercell showing the chemically complex atomic arrangement in the M-sites. (reprinted with permission from [81]) (d) XRD patterns of the starting powder mixture and the samples synthesized at 1400°C, 1500°C and 1600°C. (reprinted with permission from [35]).

[76,77]. In SHS, reagents were mixed and locally preheated to ignition temperature to initiate a spontaneous self-sustaining exothermic reaction that propagated between reagents and ultimately obtained the desired solid product. For instance, Fully dense polycrystalline Ti_3AlC_2 - Ti_2AlC dual MAX composite was successfully synthesized by spark plasma sintering (SPS) (Figure 3(a1)). In addition, Ti_3AlC_2 is the main crystalline phase with weight fraction 68% whilst 32% of the residual phase was Ti_2AlC (Figure 3(a2)) [78].

Akhlaghi et al. [79] prepared Ti_3AlC_2 using titanium, aluminum and carbon (graphite) powders by mechanical activation self-propagating high-temperature synthesis process. At first, Due to its low melting point (660°C), Al was surrounded by the Ti and C particles. At the interface between titanium particles and graphite flakes, an exothermic reaction occured between Ti and C, resulting in the formation of TiC particles. Additionally, this process promoted the generation of a Ti-Al liquid phase. At 1120°C, Then TiC particles dissolved in molten Ti-Al, and Ti_3AlC_2 phase began to nucleate. The schematic synthesis during the formation of Ti_3AlC_2 MAX phase was shown in (Figure 3(b))

$$Ti + C \rightarrow TiC(s) \quad (4)$$

$$Ti + Al \rightarrow TiAl(l) \quad (5)$$

$$2TiC + TiAl(l) \rightarrow Ti_3AlC_2 \quad (6)$$

Nowadays, the high-entropy ceramics (HECs) have received growing attentions. As for M_2SnC (M = Ti, V, Nb, Zr, Hf) high-entropy MAX phase, which indicates a chemically complex atomic arrangement in the M-layers (Figure 3(c1–c2)). Bao et al. [35] prepared high entropy M_2AlC-MC (M = Ti, Zr, Hf, Nb, Ta, Al and graphite) composites by HP method using Ti, Zr, Hf, Nb, Ta as raw materials. HP is a densification process that simultaneously applies heat and uniaxial pressure to the dense powder or body contained in the mold, thereby reducing porosity. With the increase of temperature, the Al-rich

eutectic phase gradually disappeared, indicating that the dissolution between the metals occurred, and at 1600°C, M_2AlC and MC phases were formed (Figure 3(d)). The successful dissolution of five transition metal elements in the M_2AlC MAX phase and MC carbide was confirmed. However, the formation and partial leakage of transitional aluminized eutectic phase during sintering resulted in certain loss of metal elements, especially Al atoms. With the change of the distribution of metal elements, Al vacancy leads to the delocalization of atoms and large lattice strain leads to the decline of fracture toughness.

Qiao et al. [80] prepared $((Mo_{0.25}Cr_{0.25}Ti_{0.25}V_{0.25})_3AlC_2)$ high-entropy MAX phase powder by two-step solid phase reaction method to avoid the volatilization of Al element at high temperature. Firstly, all kinds of metals and C powder were uniformly mixed according to the ratio of $M(Mo_{0.25}Cr_{0.25}Ti_{0.25}V_{0.25})$:Al:C = 3:1.4:1.9, sintered at 1600°C/3 h, and then Al powder was added for secondary sintering at 1400°C/1 h. The final high entropy MAX phase powder was obtained and the consumption of Al was effectively reduced.

Because of the binary transition metal carbides like TiC present as impurities in the final product, achieving high-purity MAX phases is challenging. The distinct mechanisms of the SPS process lead to almost full densification at lower temperatures and shorter sintering durations compared to traditional hot pressing.

The SPS process [82] allowed in situ synthesis of MAX phases from starting elemental powder such us Ti, Al, C. Also, Near monolithic MAX phase containing 95 wt.% Ti_3AlC_2 and 5 wt.% TiCx was synthesized at 1350°C with an applied pressure of 50 MPa. [83]. The evolution of impurity phase TiCx may be related to the outward diffusion and detachment of Al at high temperatures. The evaporation loss of Al leads to the transformation of hexagonal Ti_3AlC_2 ($TiAl_{0.33}C_{0.67}$) into sub-stoichiometric cubic TiC_x.

$$TiAl_{0.33}C_{0.67} \rightarrow TiC_{0.67} + 0.33Al(\uparrow) \quad (7)$$

In addition, Yunus et al. [84] synthesized phase-pure Ti_3AlC_2 MAX phases with purity exceeding 99% using (SPS) technology employing commercial-grade Ti, Al, and C. By adding a 20% excess of Al in the raw materials, which compensated for Al evaporation at high temperatures, thus enhancing the purity of the MAX phase. Even in an Ar environment at temperatures exceeding 1500°C, the MAX phase exhibited good high-temperature thermal stability.

Through an overview of the formation mechanism of bulk MAX phases, it is evident that multiple intermediate phases, such as MX (TiC), MY (Al_3Ti), AX (SiC), are formed during MAX phase synthesis. Scholars have found an oriented relationship between TiC and Ti_3AlC_2 due to their interface forming coherent boundaries [85]. This confirmed TiC as the primary intermediate phase influencing MAX phase formation. Meng et al. [86] compared the phase compositions of samples prepared using and 1 Ti: 1 Si: 2 TiC powder, which exhibited higher Ti_3SiC_2 content and lower intermediate phase content (TiC and Ti_5Si_3) than those prepared with 3 Ti: 1 SiC: 1C powder.

The M-A bonds between $M_{n+1}X_n$ layers and the A layers are weaker compared to the M-X bonds within the $M_{n+1}X_n$ layers. This enables the embedding of A layers into the M_xX_y compounds, allowing for the preparation of MAX phases. Han et al. [87] utilized a TiC_x (x = 0.6)/Al powder mixture as the starting material and employed hot-pressing sintering to fabricate Ti_3AlC_2. Polycrystalline Ti_3AlC_2 was successfully synthesized at 25 MPa at 1000°C, which significantly shortened the synthesis time and processing temperature, reduced the intermediate phase, and improved the purity of MAX phase.

The mechanism behind MAX phase formation involved the diffusion of A-site elements to ordered vacancies in MX, resulting in the creation of the MAX phase. The formation temperatures for bulk and powder MAX phases were both above 1000°C. However, for thin film MAX phases, the formation temperature notably decreased, ranging between 500–900°C. By employing sequentially deposited M/A/X metal layers in nanostructured films, the annealing temperature for MAX phases was further reduced. Through the deposition of intermediate phase MX/A and prolonging the annealing duration, Ti_2AlC can be formed at a minimum of 550°C. As the 'n' value increases within MAX phases, further diffusion reactions between elements were required, thereby elevating the formation temperature of the MAX phase. For the synthesis of high entropy MAX phase, the main problem is the formation and removal of impurity phase, the formation mechanism is similar to that of conventional MAX, first forming high entropy carbide, and then reacting with Al solid solution to form high entropy MAX phase. High entropy MAX phase can be prepared by magnetron sputtering, and its formation temperature can be significantly reduced, but how to control the formation of impurity phase is the main problem.

Up to now, synthesizing pure MAX coatings has remained a challenging task due to their highly ordered crystalline structure and potential growth of competing compounds, The addition of intermediate phases(MX) in raw materials can reduce the formation temperature of MAX phases, mitigate A-site element evaporation, and enhance MAX phase purity.

Table 1. Oxidation behavior of MAX phases under Air.

Specimen	Preparation technology	Temperature (°C)	Exposure Time (h)	Oxidation products	Oxide thickness (μm)	Msss change	Refs
Ti_2AlC	SPS	1200	50	TiO_2/Al_2O_3	8	4 mg/cm^2 for 1000 h	[34]
Cr_2AlC	Arc/sputter technology	1000	40	$(Cr,Al)_2O_3$	0.39	0.0162 mg/cm^2 for 1 h	[44]
Cr_2AlC	Magnetron sputtering	1100	1	$Al_2O_3 + Cr_2O_3$	0.8	3.7 mg/cm^2 for 1h	[89]
V_2AlC	Magnetron sputtering	600	0.5	$VO_2 + V_2O_5 + Al_2O_3$	1	–	[43]
Ti_2AlC	Magnetron sputtering	1000	0.5	(α-Al_2O_3 + R-TiO_2/α-Al_2O_3/TiO_2)	20	5.90 mg/cm^2 for 0.5 h	[90]
Cr_2AlC	FAST/SPS	1300	1	α-Al_2O_3	10	–	[91]
YSZ-Ti_2AlC	APS	1300	500	α-Al_2O_3	37–40	6.5 mg/cm^2 for 500 h	[92]
Ti_2AlC	HP	1300	120	TiO_2/Al_2O_3	17	–	[93]
$Ti_2(Al_{0.6}Sn_{0.4})C$	Magnetron sputtering	700	10	$TiO_2/Al_2O_3/SnO_2$	–	–	[94]
$(Ti_{0.9}Nb_{0.1})_3AlC_2$	HP	1200	15	Al_2O_3, TiO_2 Nb_2O_5	–	–	[95]
$Ti_3Si_{0.9}Al_{0.1}C_2$	HP	1350	20	$Al_2TiO_5/TiO_2/TiO_2 + SiO_2$	648	–	[96]

3. Oxidation of the MAX phases in air

The MAX phase oxidation has been under investigation since 2001 [28]. Oxygen resistance stands out as a critical factor for the MAX phase's application as high-temperature materials. High-temperature antioxidant materials typically establish a protective layer on the surface, mitigating further oxidation. Oxidation of alloy or composite materials generally encompasses two processes: the dissolution of oxygen and the formation of oxidation scales. This oxidation process usually initiates with thermodynamically controlled surface reactions, succeeded by the growth of the oxide film. Currently, only three oxides—silicon dioxide (SiO_2), chromium oxide (Cr_2O_3), and alumina (Al_2O_3)—have proven sufficient for forming a dense protective layer for prolonged use at 900°C. Among these, alumina has emerged as the most frequently reported oxide offering adequate protection for long-term high-temperature applications within the MAX phase. In general, the oxidation reaction of MAX can be expressed by the following formula:

$$M_{n+1}AX_n + bO_2 = M_{n+1}O_x + AO_y + X_nO_{2b-x-y} \quad (8)$$

MAX phase oxidation in air primarily involves Ti-Al-C, Cr-Al-C, and Ti-Si–C, etc. The main factors influencing MAX phase oxidation behavior encompass composition, diffusion coefficient, surface roughness, grain size, texture, residual stress, thermal expansion coefficient, and more. Understanding the microstructural evolution of oxides under different time, temperature, and atmospheric conditions is crucial for a comprehensive understanding of the oxidation mechanism. Figure 4(a) illustrated the kinetic constants and activation energies of different MAX phase and high temperature oxidation resistant alloys, and Figure 4(b) showed the Gibbs forming energies of different oxides at high temperature.

Table 1 showed the oxidation properties of different MAX phases under Air.

3.1. The oxidation of Ti2AlC

Rao et al. [16] examined the crystallographic relationship between α-Al_2O_3 oxidation scale and Ti_2AlC at 1200°C. In Ti_2AlC, the Ti-C bond exhibited strength, covalency, and directionality, contrasting with the weaker Ti-Al bond. This strong Ti-C interaction diminished reactivity, leading to the preferential oxidation of Al. In the initial oxidation stages, Al diffused from the Ti_2AlC matrix, reacting with oxygen to form α-Al_2O_3 and establishing an internal oxide layer. The depletion of Al atoms in Ti_2AlC resulted in the formation of Ti-rich interlayers, acting as a barrier to outward Al diffusion.

Cui et al. [37] investigated the microstructural evolution of Ti_2AlC ceramics during oxidation in air from 900 to 1400°C. At 900°C, TiO_2 formed on the surface of Ti_2AlC through inward diffusion of O^{2-} and outward diffusion of Ti^{4+} from Ti_2AlC. However, this differs from other reports [16]. From a bond energy perspective, The surface of Ti_2AlC should preferably form Al_2O_3. It is speculated that the samples prepared by the authors may contain impurities, with a significant presence of Ti atoms on the surface, leading to the preferential formation of TiO_2. At 1000°C, α-Al_2O_3 begins forming through inward diffusion of O^{2-} and outward diffusion of Al^{3+} from Ti_2AlC. The oxidation of Ti_2AlC can be summarized by the following reactions:

$$Ti_2AlC + xO_2 \rightarrow Ti_{2x}AlC + xTiO_2(\text{rutile}), x \leq 0.051(T < 940^\circ C) \quad (9)$$

$$Ti_2AlC + \frac{15}{4}O_2 \rightarrow 2TiO_2(\text{rutile}) + \frac{1}{2}\alpha Al_2O_3 + CO_2$$
$$\Delta V = 59.0\%,\ \Delta m = 56.4\%(T > 940^\circ C) \quad (10)$$

Due to the weak bond of Al in the Ti_2AlC structure, Al^{3+} migration from the Al atom plane in the layered structure of Ti_2AlC is easier than for Ti^{4+}. Therefore, in the inner part of the oxide scale, increasing numbers of

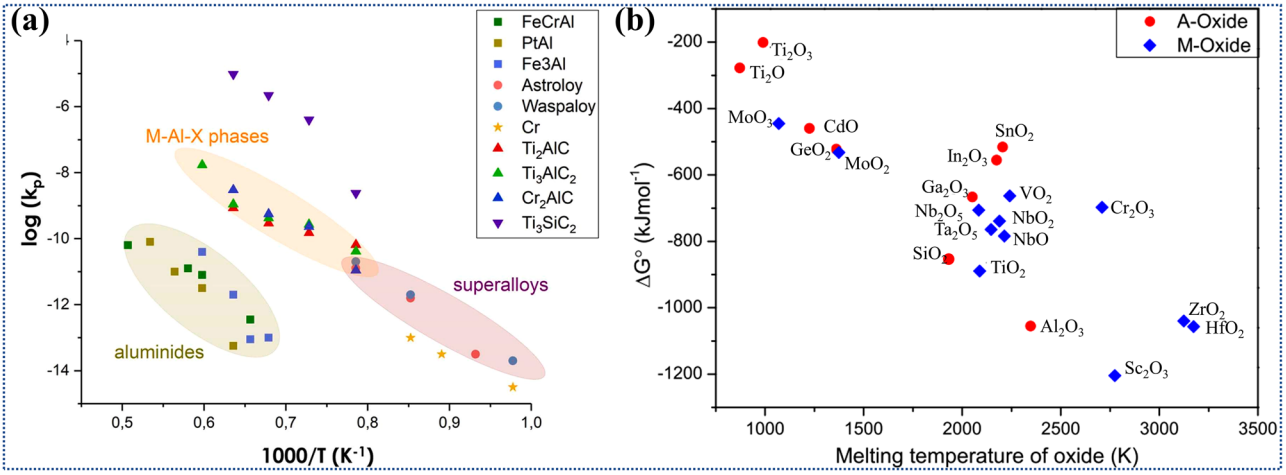


Figure 4. (a) Comparison of MAX phases parabolic kinetic constant and activation energy with high-temperature oxidation resistant alloys ones(reprinted with permission from [88]) (b) Standard Gibbs free energy of oxide formation for selected MAX phase constituents(reprinted with permission from [41]).

α-Al_2O_3 grains nucleated. During high-temperature oxidation below 1300°C, the microstructural development of Ti_2AlC involves the gradual formation of an externally discontinuous TiO_2 layer and an internally dense continuous a-Al_2O_3 layer. Heating to 1400°C results in the formation of an outer layer consisting of a mixture of TiO_2 and Al_2TiO_5, along with a fractured inner layer of α-Al_2O_3. Upon heating to 1200°C and subsequent cooling to room temperature, two types of planar defects within the surface TiO_2 grains are revealed: twinning with (200) planes and stacking faults bounded by partial dislocations. Thermal stresses generated by the thermal expansion mismatch among TiO_2, α-Al_2O_3, and Al_2TiO_5 phases in the oxide layer are relieved within the TiO_2 particles. However, crack propagation occurs within the TiO_2 grains upon heating to 1400°C and cooling to room temperature, due to thermal expansion mismatch among phases in the oxide layer, the high anisotropy of thermal expansion in Al_2TiO_5, and volume changes associated with the Ti_2AlC oxidation process.

3.2. The oxidation of Cr2AlC

Studies on the Cr-containing MAX phase have also been conducted. Cr_2AlC, as a member of the M_2AlC family, exhibits the highest bulk modulus due to its maximum Cr-C bond energy compared to other transition metal materials (M = Ti, V, Nb, Ta).

Hajas et al. [97] explored the isothermal oxidation behavior of Cr_2AlC coatings on alumina substrates in the temperature range of 1230°C to 1410°C. Al depletion and oxidation of Cr carbides led to the formation of CO gas and Cr_2O_3. The concurrent occurrence of gas formation, along with Al and Cr depletion, contributed to the substantial void formation observed in the Cr carbide interlayer (Figure 5(a1)). The alumina scale exhibited a wide region where a $(Al,Cr)_2O_3$ solid solution formed, accompanied by Cr carbide precipitation (Figure 5(a2)). Additionally, Zuber et al. [88] summarized the oxidation mechanism of Cr_2AlC in an air environment (Figure 5(b)).

Wang et al. [44] discussed the oxidation mechanism of Cr_2AlC coatings, emphasizing the characterization of oxide scales and microstructural evolution during oxidation. At 900°C, selective oxidation of Al resulted in the formation of a dense, continuous outermost layer of Al_2O_3. This Al depletion-induced transformation changed Cr_2AlC into Cr_7C_3 and Cr_3C_2 phases. At 1000°C and 1100°C, besides the formation of Cr_7C_3 and $Cr_2(C,N)$, a mixed oxide layer of Cr_2O_3 and Al_2O_3 was observed. After 40 h oxidation at 1000°C, Al enrichment occurred at the coating/substrate interface. With the oxidation temperature reaching 1100°C, the enriched Al interface layer transformed into a dense α-Al_2O_3 layer, further enhancing the oxidation resistance of the Cr_2AlC MAX phase coating. For both stage I and stage II, the rate of mass gain in the Cr_2AlC coatings was larger in stage I than in stage II, as no perfect oxide scale formed during stage I (Figure 5(c1)). The oxidation process was shown in (Figure 5(c2)).

Sun et al. [98] investigated the oxidation behavior of Ti_3SiC_2 in air within the temperature range of 900 ~ 1200°C. Beyond 1000°C, the oxide layer exhibited a two-layer structure: a coarse-grained outer layer of TiO_2 (rutile) and a fine-grained inner layer of TiO_2 and SiO_2. Between 1100°C and 1200°C, the oxide layer gradually transformed into an outer layer of coarse-crystal TiO_2 and an inner layer of discontinuous coarse-crystal SiO_2.

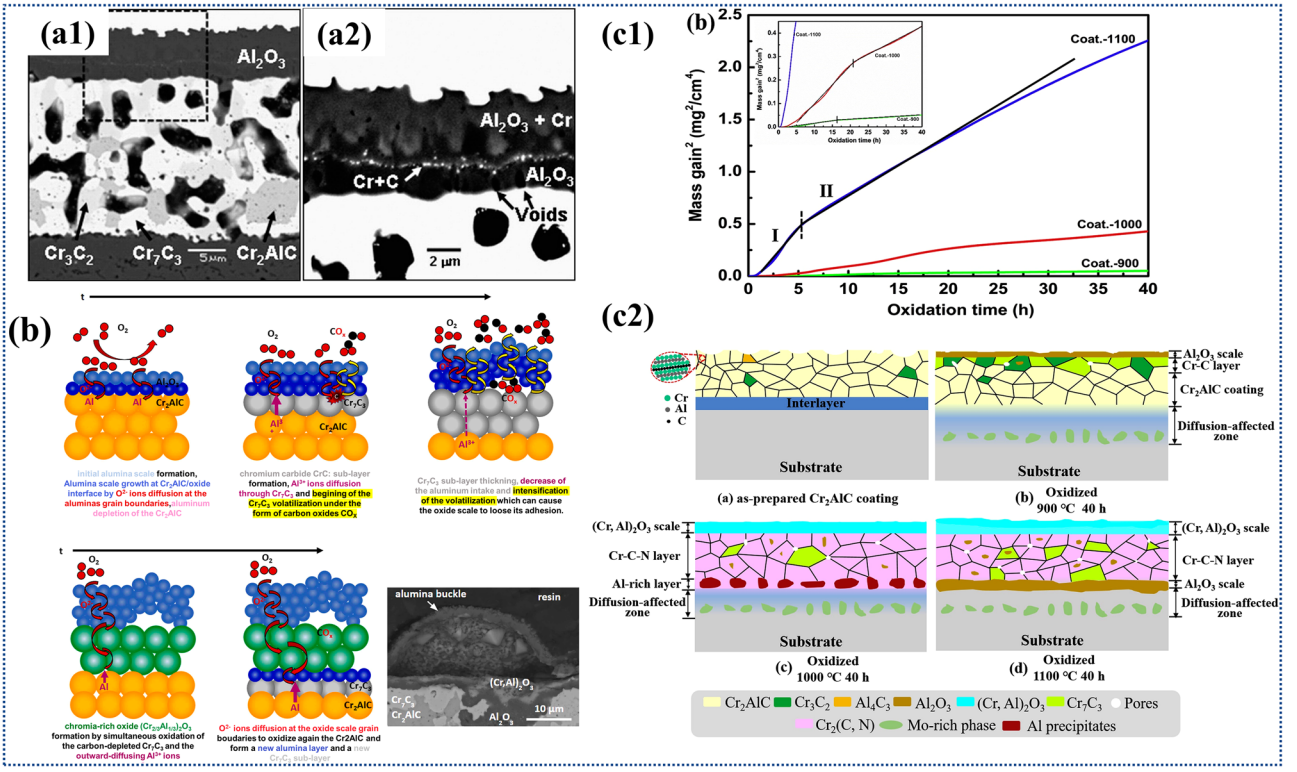


Figure 5. (a1) Cross sectional analysis of Cr_2AlC film oxidized at 1320°C cross sectional BSE image (a2) magnification of the Al_2O_3 scale marked in (a) (reprinted with permission from [97]). (b) Schematic of the high-temperature oxidation mechanism of Cr_2AlC in air with a final microstructure of a sample oxidized 1000 h at 1000°C (reprinted with permission from [88]) (c1) Square of mass gain per unit surface area as a function of time (the inset representing the detail in the initial stage). The vertical dash line and the black line show the dividing point of the oxidation stage and the fitting results of the experimental results, respectively. (c2)Schematic diagram of the oxidation mechanism for the Cr_2AlC coatings at different temperatures (reprinted with permission from [44]).

The oxidation process was governed by the inward diffusion of oxygen and the outward diffusion of titanium, CO, or SiO.

3.3. The effect of grain size on MAX phases

The size of the grain determines the number of grain boundaries. These boundaries serve as channels for atomic diffusion in the MAX phase, and an increased number of grain boundaries facilitates the diffusion of the active A-site atom Al in the MAX phase, ensuring the rapid formation of a protective oxide film [99–101]. Drouelle et al. [101] fabricated coarse and fine crystal Ti_3AlC_2 samples using spark plasma sintering and hot isostatic pressing. In the temperature range of 900–1000°C, alumina formed on the surface of the fine crystal sample, whereas a mixed (TiO_2-Al_2O_3) unprotective layer formed on the surface of the coarse-crystal sample.

Yu et al. [100] investigated the oxidation behavior of fine crystalline (FG) and coarse crystalline (CG) Ti_2AlC samples at 800°C, 900°C, 1000°C, and 1100°C in air. The results indicated a faster oxidation rate for coarse crystal samples. In FG-Ti_2AlC bulk samples, a dense and protective Al_2O_3 layer formed on the surface (Figure 6(a1)). In contrast, the CG-Ti_2AlC sample exhibited the formation of a thick TiO_2 layer on top of the discontinuous Al_2O_3 layer (Figure 6(a2)). Moreover, irrespective of the temperature, the weight gain per unit surface area of CG-Ti_2AlC was two orders of magnitude higher than that of FG-Ti_2AlC (Figure 6(a3–a4)). CG-Ti_2AlC did not convert directly to TiC but to both Ti_3AlC_2 and TiC. As the density of Ti_2AlC (4.067 g cm^{-3}) was lower than that of Ti_3AlC_2 (4.247 g cm^{-3}), the conversion of Ti_2AlC to TiCx (4.933 g cm^{-3}) resulted in more severe volume shrinkage [102]. The volume shrinkage elongated holes, partially filled with α-Al_2O_3. The stress induced by volume shrinkage created surface cracks, facilitating the inward diffusion of oxygen and worsening the oxidation resistance of the CG-Ti_2AlC block.

Some researchers have investigated the oxidation resistance of monocrystalline materials, deliberately avoiding the influence of grain boundaries. Zuber et al. [99] conducted a study on the high-temperature oxidation of bulk single crystal, fine, and coarse-grained polycrystals of Cr_2AlC from 800°C to 1000°C. The grain

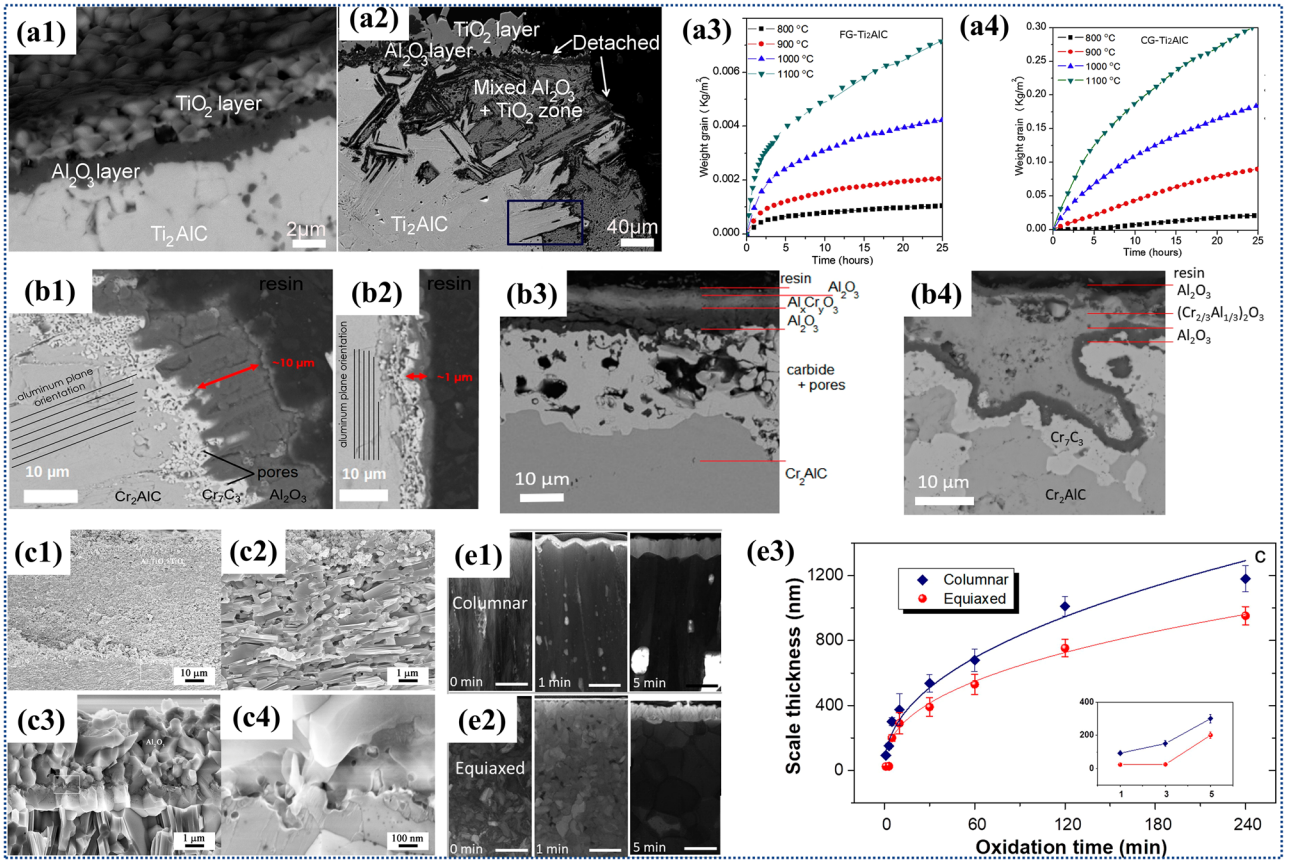


Figure 6. BSE-SEM micrographs of the oxidized surface of FG (a1) and CG-Ti_2AlC (a2); (a3) Weight gain per unit surface area of Ti_2AlC as a function of oxidation time at 800, 900, 1000 and 1100°C for oxidation in air of FG-Ti_2AlC bulk samples and (a4) CG-Ti_2AlC bulk samples (reprinted with permission from [100]). (b1) side, (b2) top of the plates of an oxidized single crystal sample at 1200°C for 2 h. Cross-sectional SEM micrographs of (b3) a single crystal sample oxidized at 1500 °C for 2 h; (b4) a fine-grained sample oxidized at 1000°C for 1000 h. (reprinted with permission from [99]). Fracture surfaces of scales grown on textured Ti_3AlC_2 ceramics: (c1) and (c2) TTS-type sample (1373 K), (c3) and (c4) TSS-type sample tested at 1473 K. Figs. (c3) and (c4) are the magnified regions marked by a rectangle in Figs. (c1) and (c2) respectively. (reprinted with permission from [103]). STEM bright field images (Helios) of the cross-sections of columnar (e1) and equiaxed (e2) grained Cr_2AlC coatings before oxidation and after oxidation at 1100°C from 1 to 5 min. (e3)Variation of the oxide scale thickness with oxidation time and corresponding power lawfit in the equiaxed and columnar grained samples. The inset in (e3) shows the initial scale thickness from 1 to 5 min. (reprinted with permission from [104]).

orientation and size influenced the thickness of alumina. Due to the layered structure of MAX phases, atoms migrate more easily along layers than through layers. Therefore, the oxidation process of MAX phases is anisotropic. As shown in (Figure 6(b1–b2)), in single crystal samples, the upper part of the plates, corresponding to a basal plane orientation parallel to the surface, developed a thinner oxide scale compared to the sides of the plates, which corresponds to a basal plane orientation perpendicular to the surface. Despite differences in material structure, the oxidized oxide layer exhibited similar characteristics, with a continuous alumina layer and Cr_7C_3 sublayer formed on the surface of Cr_2AlC.

The difference in the slow diffusion of chromium and the rapid diffusion of aluminum, along with the evaporation of carbon during oxidation, could create pores and Kirkendall voids (Figure 6(b3)). For fine crystals, the abundance of grain boundaries facilitates easy diffusion paths for aluminum atoms, preventing the depletion of Al in MAX phase grains under the oxide layer. A mixed aluminum and chromium oxide layer is likely sandwiched between two alumina layers above the Cr_7C_3 subscale and Cr_2AlC substrate (Figure 6(b4)).

3.4. The effect of texture on MAX phases

Due to the layered crystal structure of MAX phases, they exhibit different behaviors along various crystal orientations. If favorable external conditions, such as uniaxial pressure or magnetic fields, are applied during the preparation of the MAX phase, flaky grains can be preferentially arranged in a specific direction to

form a textured MAX phase with anisotropy. Therefore, the texture of the MAX phase offers a potential means to enhance its oxidation resistance without altering its chemical composition.

Xu et al. [103] investigated the oxidation resistance of textured Ti_3AlC_2 ceramics in the temperature range of 1000 ~ 1300°C. The textured top surface (TTS), parallel to basal planes and orthogonal to the c-axis, exhibited a surface oxide composed of a porous mixture of TiO_2 and Al_2TiO_5 when formed at a temperature of 1473 K (Figure 6(c1–c2)). Due to the preferential outward diffusion of aluminum atoms on the (000 l) base surface, a dense passivated alumina layer quickly formed. Consequently, a distinctly different microstructure was observed on TSS, with a surface composed of dense alumina (Figure 6(c3–c4)). The results indicated significant anisotropy in the oxidation process, with the samples demonstrating good oxidation resistance when tested along the c-axis.

The impact of nanoscale morphology on the oxidation behavior of MAX phase coatings has not been thoroughly investigated. Chen et al. [104] compared the oxidation behavior of Cr_2AlC MAX phase coatings with columnar and equiaxed morphologies. After oxidation at 1100°C for 240 min, the Cr_2AlC MAX phase coatings with equiaxed grains exhibited a 20% lower scale thickness and a 52% larger scale grain size compared to the coatings with columnar grains (Figure 6(e1–e2)). The scale thickness increased gradually with prolonged oxidation time for both samples. Additionally, the scale thickness of the equiaxed coating was smaller than that of the columnar coating for all investigated oxidation times (Figure 6(e3)).

3.5. The effect of surface conditions on MAX phases

Based on the preceding analysis, the oxidation kinetics of the MAX phase is influenced by its microstructure. Additionally, the surface status of the sample also significantly affects the formation of surface oxide film. Some studies have indicated that a damaged Ti_2AlC MAX phase surface underwent separation and oxidation, leading to the rapid accumulation of large rutile crystals, which severely impacted the oxidation resistance of the MAX phase. Consequently, the impact of sample surface quality on their oxidation behavior has been extensively explored [34,105].

Badie et al. [105] investigated the oxidation behavior of Ti_2AlC with varying roughness and observed a significant influence of surface roughness on oxide morphology. Ti_2AlC samples with different roughness exhibited varying degrees of cavities on their surfaces. The presence of cavities resulted in a low accumulation of Al_2O_3, facilitating the diffusion of Ti ions to the outer grain boundary and thus forming TiO_2 on top of Al_2O_3. As roughness increased, the amount of TiO_2 gradually rose (Figure 7(a1–a4)). However, due to the substantial undulations on the substrate surface before oxidation, the total length of Al_2O_3 was highest after the oxidation of the sample with the greatest roughness. Consequently, more Al was depleted in this case. When the critical amplitude of undulations before oxidation is higher, the oxide film began to wrinkle, leading to local failure of the Ti_2AlC/Al_2O_3 interface. In addition, the separation oxidation mechanism of Ti_2AlC, and the main triggering factors and corresponding solutions to mitigate it were investigated [34]. As depicted in Figure 7, the rough surface of the sample with a wavy profile exhibited an uneven stress distribution. With the progression of the oxidation process, the interface between the growing oxide and Ti_2AlC experienced significant tensile stress, resulting in the warping of the oxide layer (Figure 7(b1)). As the wave amplitude of the oxide layer increased, the matrix/oxide interface became stratified (Figure 7(b2)). The gap between Ti_2AlC and the layered oxide had a low oxygen partial pressure, leading to abnormal growth of TiO_2 particles (Figure 7(b3–b4)). This was primarily due to the MAX phase's inability to continuously form a protective Al_2O_3 oxide layer. Consequently, a large rutile-TiO_2 gradually filled the gap. The excessive growth of rutile was detrimental to the system's integrity (Figure 7(b5–b6)), resulting in a substantial mass gain during oxidation. A schematic representation of oxide scale rumpling/buckling, blistering, and subsequent breakaway oxidation is shown in (Figure 7(b7)).

Excessive overgrowth of rutile TiO_2 is detrimental to the integrity of the system. It is helpful to suppress the abnormal growth of TiO_2 by reducing surface roughness. In addition, the modification of MAX phase elements to inhibit the diffusion of Ti elements and abnormal oxidation is a future research focus.

MAX phases, including Ti_2AlC, Ti_3AlC_2, and Cr_2AlC, with A-site elements being aluminum, display excellent air oxidation resistance. This is attributed to the formation of a dense, peel-resistant, and protective Al_2O_3 layer. Varied oxygen partial pressures and oxide formation energies lead to the preferential oxidation of aluminum, resulting in distinct oxide layer structures. Ti-containing Al-based MAX phases show a discontinuous outer layer of TiO_2 and a continuous inner layer of Al_2O_3, while Cr_2AlC forms a $(Cr,Al)_2O_3$ solid solution layer. Consumption of A-site elements induces structural transformations in MAX phases, forming residual

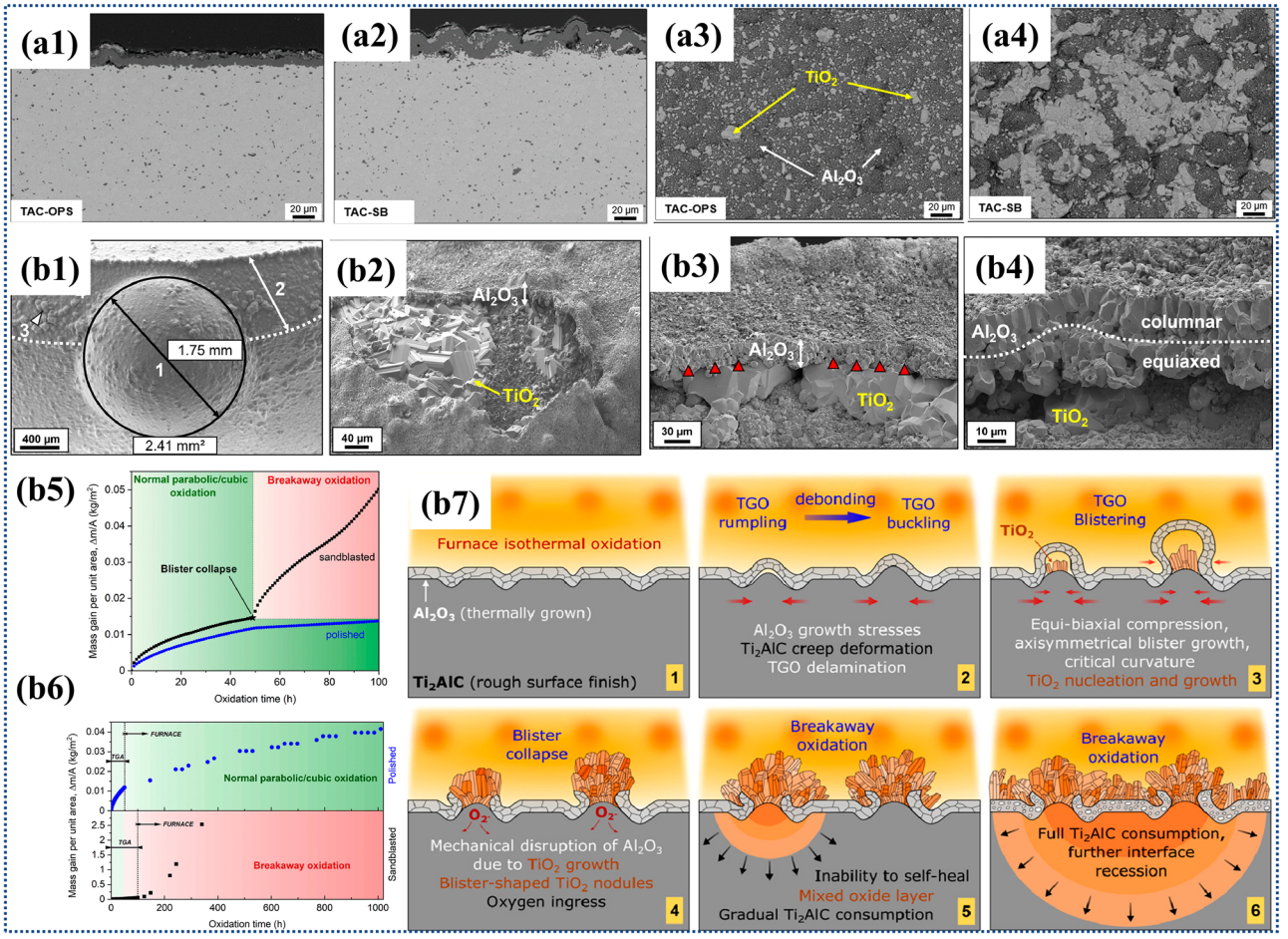


Figure 7. Cross-sectional BSE images of oxidized Ti_2AlC samples with different surface finish: (a1, a3) polished to 50 nm colloidal silica, (a2, a4) sandblasted with F36 alumina particles. Oxidation conditions were 1200°C, 50 h in static air (reprinted with permission from [105]), (b1)Oxide microstructure and morphology of the polished sample after 1274 h at 1200°C, micrograph of the large white blister (b2) presence of large TiO_2 grains growing underneath, (b3) pressure exerted by rutile grains on the Al_2O_3 scale and (b4) Al_2O_3 scale morphology. Mass gain curves for polished and sandblasted Ti_2AlC samples oxidized at 1200°C, retrieved from (b5) TGA experiments and (b6) long-term furnace cycling experiments, (b7) Schematic representation of oxide scale rumpling/buckling, blistering and subsequent breakaway oxidation (reprinted with permission from [34]).

carbide coatings (e.g. TiC, Cr_3C_2, Cr_7C_3) beneath the oxide layer. Further oxidation of these carbides generates voids within the residual coatings, compromising mechanical and oxidative properties. Increasing the A-element content in MAX phases could reduce voids, enhancing oxidation resistance.

In contrast, the oxidation of Ti_3SiC_2 involves O internal diffusion and external diffusion of Ti, with non-selective oxidation of Si. Initially, a TiO_2 layer lacking oxygen-blocking capabilities forms, causing severe internal oxidation. A rutile-to-anatase phase transformation in TiO_2 (A-R phase transition) induces tensile stresses, forming microcracks in the coating. The formation of SiO_2 reduces interface oxygen partial pressure, facilitating gaseous SiO diffusion. Regions with high oxygen content in TiO_2 result in uneven distribution of Si-rich bubbles and SiO_2, forming a mixed oxide layer of SiO_2 and TiO_2 [98].

4. Oxidation of the MAX phases under the effect of water

Exploring the oxidative corrosion of MAX phases in water environments is crucial for expanding their applications. The corrosion resistance in aqueous environments relies on the oxide layer's stability and its interaction with water. This section offers a comprehensive overview of MAX oxidation behavior in water environments, discussing the failure mechanism and factors influencing the oxidation process. [48,93,106–116]. Table 2 showed the oxidation properties of different MAX phases under water.

4.1. Critical water environment

MAX phases, with their unique blend of ceramic and metallic properties, have become potential materials for

Table 2. Oxidation behavior of MAX phases under water.

Specimen	Preparation technology	temperature (°C)	Exposure Time (h)	Oxidation products	Oxide thickness (μm)	Mass change	Refs
Cr_2AlC	SPS	1400	40	$Al_2O_3/(Cr,Al)_2O_3$	14 ± 1	8×10^{-8} mg/mm^2/s	[88]
Ti_3SiC_2	HP	360	24	$TiO_2 + SiO_2$	13	0.0343 mg/cm^2 for 300 h	[106]
Cr_2AlC	Magnetron sputtering	1000	1	α-Al_2O_3	0.6	25.1 mg/cm^2 for 1.7 h	[107]
Ti_2AlN	Cathodic arc/sputter	750	80	Al_2O_3/TiO_2	7	6130 mg/cm^2 for 40 h	[108]
Ti_2AlC	HP	1400	12	$Al_2TiO_5 + \alpha$-Al_2O_3	10	3.24 mg/cm^2 for 24 h	[111]
Ti_2AlC	HP	1300	120	$TiO_2 + Al_2O_3$	14 ± 2	6.0×10^{-11} kg^3/m^6/s	[93]
Ti_2AlC	arc/magnetron sputtering	1100	1/6	$TiO_2 + Al_2O_3$	13.0	1.94 mg/cm^2 for 10h	[90]
Ti_2AlC/TiC	Magnetron sputtering	1000	4.2	$Al_2O_3 + TiO_2$	3.6	3.7 mg/cm^2 for 1h	[110]
Ti_2AlC	Magnetron sputtering	750	200	$TiO_2 + Al_2TiO_5$	–	–	[114]
Ti_3SiC_2	HP	700	95	$SiO_2 + TiO_2$	69	24.2×10^{-2} ug/mm^2/h	[115]

nuclear applications. Hydrothermal corrosion resistance is a key factor for MAX phase application in pressurized water reactors (PWR) under normal operation conditions [106]. At present, the study of MAX phase in critical water environment mainly focuses on corrosion mechanism and microstructure evolution.

Ti_3AlC_2, Ti_2AlC, Ti_3SiC_2, and Cr_2AlC exhibit good performance in high-temperature air. However, it is unknown if these materials perform equally well under prolonged low-water reactor cooling conditions. To assess their suitability for the light water reactor environment (LWR), Ward et al. [109] investigated their corrosion properties under simulated primary water conditions. In a low-oxygen environment ($<$ 5 ppb), Ti-based MAX phases with A-elements Al and Si failed to form protective oxidation layers. Interestingly, Cr_2AlC forms Cr_2O_3 on its surface, demonstrating superior oxidation resistance. Nano-sized pores exist in residual layers beneath the oxide, seemingly not affecting oxidation resistance. Additionally, Fe in the reaction vessel forms discontinuous TiFeO3 on the surface, apparently not influencing the oxidation resistance of the MAX phase.

The dissolved oxygen content in water significantly influences the oxidation of MAX phases in a water environment. Zhu et al. [106] conducted three experimental groups with varying levels of dissolved oxygen content to study the corrosion behavior of Ti_3SiC_2. Using double Cs-corrected STEM, they directly observed the corrosion-induced Si-layer escape of Ti_3SiC_2 and, at an atomic scale, witnessed the transformation of Ti_3SiC_2 MAX phase into Ti_3C_2 nanosheets (Figure 8(a)). Increasing the dissolved oxygen content accelerated corrosion (Figure 8(b–c)). In addition, the coexistence of bipyramidal anatase and nanocuboid rutile particles in the corrosion layer (Figure 8(d–e)). The reaction process of Ti_3SiC_2 with water was as follows:

$$Ti_3SiC_2(s) + 2H_2O(aq) = Ti_3C_2(s) + SiO_2(s) + 2H_2(g) \quad (11)$$

$$SiO_2(s) + 2H_2O(aq) = Si(OH)_4(aq) \quad (12)$$

$$SiO_2(s) + 2H_2O(aq) = H_4SiO_4(aq) \quad (13)$$

$$Ti_3C_2(s) + 6H_2O(aq) = 3TiO_2(aq) + 2C(s) + 6H_2(g) \quad (14)$$

Dissolved oxygen not only corroded along grain boundaries but also penetrated inside the Ti_3SiC_2 grain parallel to the Ti_3SiC_2 crystal base plane, resulting in complete separation of Ti_3SiC_2 grains. Subsequently, dissolved oxygen moved through the corrosion hole, forming larger voids. These voids interconnected along grain boundaries, forming a corrosion network. Eventually, corrosion products within the network were removed. A schematic illustration depicting the corrosion mechanism and process of Ti_3SiC_2 MAX phase was presented in Figure 8(f).

4.2. Steam environment

In various energy systems, such as coal-fired power plants and nuclear stations, pure steam is a common environment. In efforts to enhance thermal efficiency, steam temperature and pressure have significantly increased over the years, bringing attention to steam oxidation issues. Water vapor critically influences oxidation processes, altering oxide layer composition and structure while accelerating oxidation rates.

Various hydrogen-containing substances, especially hydroxide ions, produced in high-temperature steam environments, exhibit higher diffusion coefficients, smaller sizes, and lower electric charges, resulting in faster oxidation rates in steam compared to oxygen at the same temperature.

Tang et al. [111] investigated the oxidation behavior of bulk Ti_2AlC ceramic in steam at temperatures ranging from 1400°C to 1600°C. As the temperature raised, oxide stratification occurred, and a substantial amount of volatile gas gradually transformed the dense oxide layer into a loose porous structure (Figure 9(a1–a4)). During steady-state oxidation, outward diffusion of Ti and C through grain boundaries of the α-Al_2O_3 scale led to the

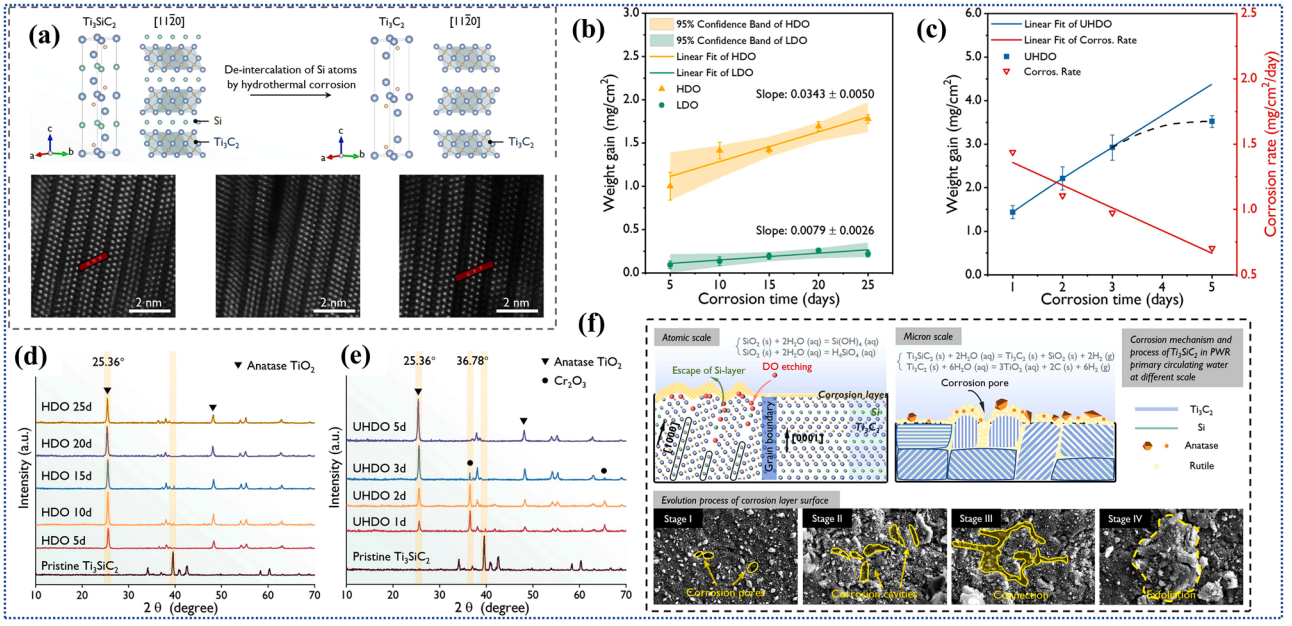


Figure 8. (a) The schematic illustration of the transformation from Ti_3SiC_2 to Ti_3C_2 under simulated PWR conditions. Evolution of the mean weight gain as a function of the corrosion time of Ti_3SiC_2 bulk sample in (b) LDO, HDO groups and (c) UHDO groups. XRD characterization on the surface of corroded Ti_3SiC_2 samples in (d) HDO and (e) UHDO groups. (f) Schematic illustration of the corrosion mechanism and process on the Ti_3SiC_2 MAX phase surface at different scale (reprinted with permission from [106]).

segregation of TiO_2 at the grain boundaries of α-Al_2O_3 and the formation of gaseous CO and CO_2, respectively. The flow rates of H_2 and CO_2 in the off-gas was significantly increased compared to oxidation at 1400°C (Figure 9(a5)).

Zuber et al. [88] investigated the high-temperature oxidation of Cr_2AlC in wet air up to 1400°C. In the water environment, as the temperature increases, the Al_2O_3 protective layer folds, and the holes in the residual coating increase (Figure 9(b1–b5)). The presence of water vapor significantly increases the pressure, forming a gas mainly composed of carbon oxides due to the oxidation of chromium carbide (Figure 9(b6–b7)). In the water vapor environment, mass gain increases with temperature. Furthermore, compared to temperature, the change trend of mass gain with the increase of water vapor partial pressure is smaller (Figure 9(b8)). In the temperature range of 1000–1400°C, the activation energy is in the range of 430–530 kJ/mol (Figure 9(b9)).

Wang et al. [108] discovered differing oxidation rates for Ti_2AlN in water vapor and air. In air, the coating's uneven oxidation, attributed to large particles and impurity phases, contrasted with the uniform oxidation observed in pure steam. After 60 h of steam oxidation, an area devoid of large particles exhibited the formation of small, loose, noodle-like oxides. Hydrogen atoms presence led to accelerated corrosion. The aqueous atmosphere induced numerous defects in α-Al_2O_3 and TiO_2. Hydroxide ions, being the main point defects in vapor, diffused faster due to their smaller size than oxide ions, resulting in quicker oxidation kinetics. Additionally, outward Al diffusion and hydrogen release caused pores in oxide layers

$$H_2O(g) = H_2O(s) \tag{15}$$

$$H_2O(s) + V_{\ddot{o}} = OH_o^{\cdot} + H_i \tag{16}$$

$$2H_i + 2e' = H_2(g) \tag{17}$$

The Ti_2AlC coating's oxidation resistance in pure steam was investigated at 1000°C, 1100°C, and 1200°C with varying oxidation times [90]. Coated Zirlo substrates exhibited enhanced oxidation resistance due to a compact structure and the formation of a triple-scale oxide scale (α-Al_2O_3 + R-TiO_2/α-Al_2O_3/TiO_2). Figure 10(a1–a2) shows the oxide scale thickness reaching 8.8 μm after 30 min, and a multilayer structure was observed. Subsequently, the entire coating was consumed (Figure 10(a3–a4)). The schematic diagram is presented in (Figure 10(a5–a6)).

Tang et al. [110] noted the necessity of an effective diffusion barrier for high-temperature applications surpassing 1000°C. Figure 10(b1,b3) illustrates different oxide layer arrangements with and without a TiC barrier. Coatings lacking a barrier exhibited a double-layered oxide scale, while only one Al_2O_3-rich layer was seen in the presence of a TiC barrier. Additionally, full oxidation of the sample occurred around 240 min (Figure 10(b2)). The coating with a TiC barrier showed a

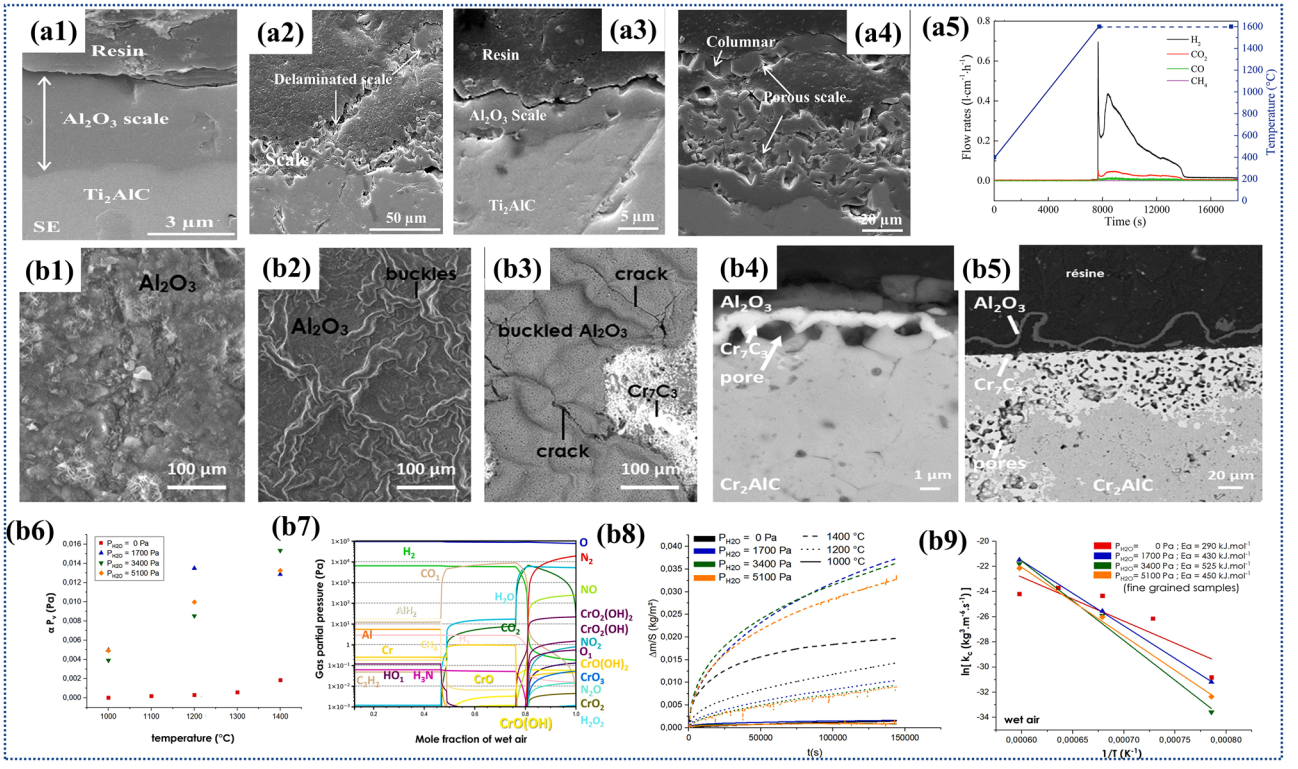


Figure 9. SEM images of typical cross section morphologies of Ti_2AlC oxidation:(a1)1400°C—1 h, (a2) 1400°C—24 h (a3) 1500°C—1 h (a4) 1500°C – 12 h (a5) Flow rates of H_2,CO_2, CO, and CH4 in the off-gas as a function of time for the Ti_2AlC samples oxidized at 1600°C(reprinted with permission from [111]). Cross-section SEM micrographs, in back-scattered mode, of a finegrained Cr_2AlC sample oxidized at: (b1) 1000°C and (b2) 1200°C during 40 h under wet air (PH2O = 1700Pa). SEM micrographs of fine-grained Cr_2AlC sample's surface oxidized at: (b3) 1400°C during 40 h under wet air (PH2O = 1700Pa), (b4)1000°C, (b5)1200°C, (b6)Evaporated gas partial pressures deduced from the volatilization constant of Cr_2AlC fine-grained samples oxidized in wet air during 40 h and in dry air during 100 h in the temperature range 1000–1400°C. (b7) CALPHAD calculations of the oxidation product's partial pressures at 1200 °C under wet air (PH2O = 5100 Pa). (b8)Normalized mass gain curves of fine-grained Cr_2AlC samples oxidized during 40 h at T = [1000; 1200; 1400]°C and at PH2O = [1700; 3400; 5100] Pa (b9) Arrhenius plots of cubic kinetic constants of Cr_2AlC fine-grained samples after 40 h oxidation in wet air in the temperature range 1000–1400°C (reprinted with permission from [88]).

slightly lower weight gain (40.9 mg/cm^2) than that without a barrier (48.7 mg/cm^2) after a 15-minute exposure (Figure 10(b4)). The schematic diagram is presented in (Figure 10(b5–b6)).

In high-temperature water vapor environment, water vapor induced the oxidation and evaporation of interface carbides, leading to higher partial pressures of carbon oxides and accelerating the oxidation of MAX phases. Simultaneously, this diminished the bond strength between the coating and the substrate. The incorporation of an intermediate layer in the coating interface design can prevent the diffusion of Al elements into the substrate, effectively enhancing the coating's lifespan and corrosion resistance. Reducing dissolved oxygen in the water environment can improve the corrosion resistance of MAX phases. When Cr-based MAX phases are exposed to water or humid environments, a protective layer of chromium oxide (Cr_2O_3) forms on the surface. This layer is highly stable and acts as a barrier to further oxidation and corrosion. In addition, chromium oxide has excellent adherence and low solubility in water, which helps to achieve protection of the base material. According to the Ellingham diagram, Cr_2O_3 exhibits a significantly negative Gibbs free energy of formation. This implies that Cr_2O_3 is thermodynamically stable across a wide range of temperatures and conditions, making it less likely to undergo reduction or other degradation reactions in aqueous environments. Overall, the oxidation of MAX phases in water environments is primarily influenced by two factors: dissolved oxygen altering the oxidation products and oxide layer structure, and the acceleration of the oxidation process by smaller hydroxide ions, promoting the hydrolysis of protective oxides such as Al_2O_3 and SiO_2. Additionally, the generation of volatile gas by-products disrupts the structure of the oxide layer.

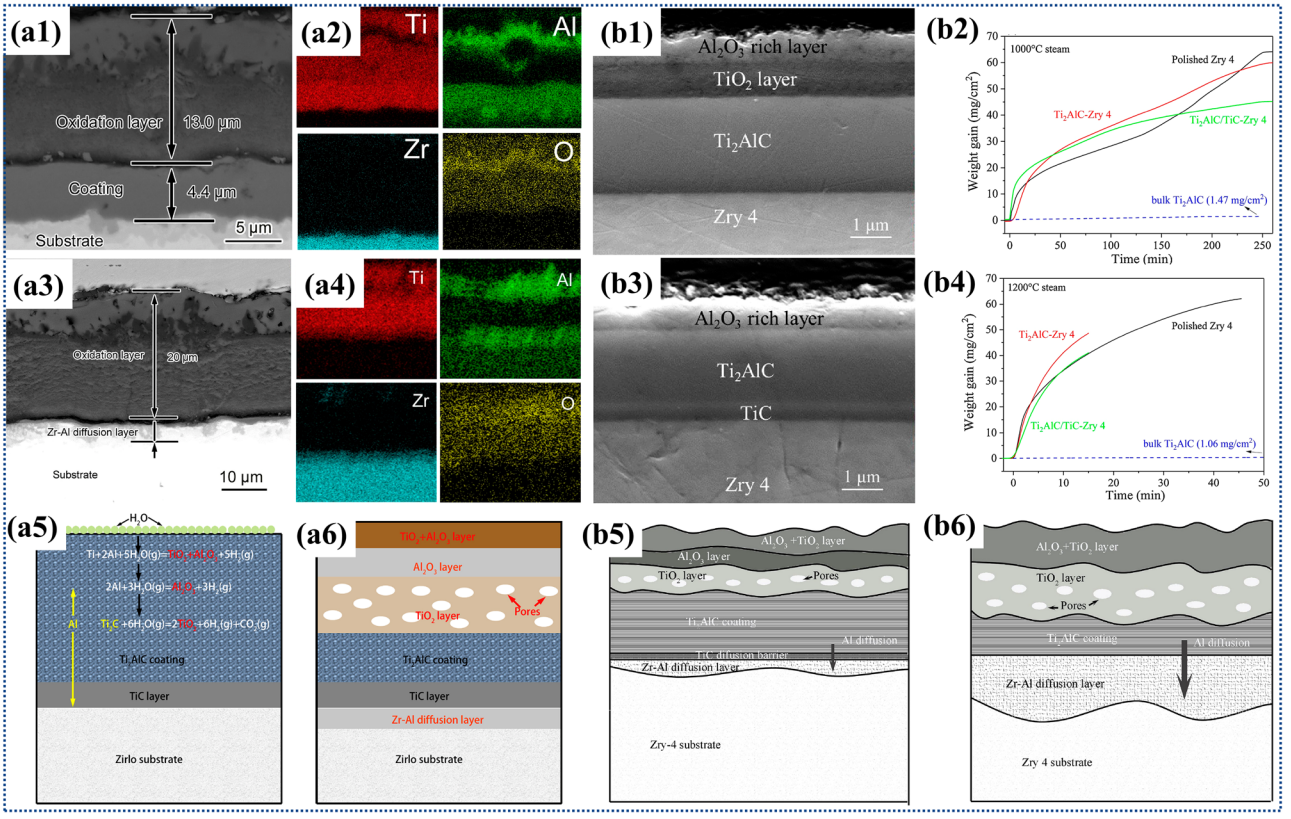


Figure 10. SEM images of cross section of coated samples after oxidation at 1000°C for 20 min (a1) and 30 min (a3) with corresponding EDS elemental mapping (a2) and (a4), respectively. Schematic diagram of cross-sectional microstructure of Ti_2AlC coated Zirlo substrate oxidized at 1000–1200°C, (a5) oxidation process and (a6) result (reprinted with permission from [90]). SEM images of cross section of coated samples after oxidation at 800°C in steam for 5 min, (b1) Ti_2AlC- and (b2) Ti_2AlC/TiC-coated Zry-4, Oxidation kinetics of bulk Ti_2AlC, polished Zry-4 substrates, and Ti_2AlC- and Ti_2AlC/TiC-coated Zry-4 at (b3) 1000°C and (b4) 1200°C in steam. Schematic of cross sectional microstructure of (b5) Ti_2AlC and (b6) Ti_2AlC/TiC coating on Zry-4 during oxidation at 800°C in steam with 5.5 μm thick coatings (reprinted with permission from [110]).

5. The corrosion behavior of MAX phases in corrosive medium

5.1. Molten salt environment

The compressor blades of aircraft engines and gas turbines are susceptible to severe corrosion from prolonged exposure to high-temperature, high-salt, and high-humidity marine environments, significantly shortening their service life. Moreover, molten salt reactors (MSRs) utilize liquid fuel in the form of molten chloride or fluoride salts as a coolant. Corrosion of these materials by molten salt can create surface pores or cracks, leading to perforation or rupture of molten salt loop pipelines.

MAX phases demonstrate remarkable chemical and physical properties—strong chemical stability, high strength at elevated temperatures, and excellent corrosion and oxidation resistance. This makes them promising under molten salt reactors [2,83,116–118].

Magnus et al. [83] synthesized 95 wt.% Ti_3AlC_2 MAX phase through spark plasma sintering (SPS) under vacuum conditions and studied its corrosion behavior in LiCl-KCl eutectic molten salt. When the Ti_3AlC_2 MAX phase is in contact with the molten salt, the chemical driving force induces the precipitation and migration of Al from the atomic plane of Ti_3AlC_2. forming a reaction layer ~80–120 μm thick (Figure 11(a1–a2)). Continuous extraction of Al from the A atom site will leave a twin and relaxed Ti_3C_2 layer, which will be spontaneously terminated by cl- ions to form stable $Ti_3C_2Cl_2$ (Figure 11(a3)). In addition, due to the action of oxygen, the in diffused O may occupy the empty A site vacated by the Al atom, thus detwinned the relaxed Ti_3C_2 layer to a non-chemical quantity of $TiC_{0.67}$ (Figure 11(a4)). Finally, the excessive Al migration led to the destruction of the MAX phase structure.

Li et al. [117] compared the corrosion of MAX phases under simulated marine environment (NaCl) and atmospheric conditions. In the atmospheric environment, Cr_2AlC exhibited superior oxidation resistance, attributed to the rapid formation of a continuous and dense Al_2O_3 layer on the sample surface. Conversely, Ti_3SiC_2 and Ti_2AlC formed porous TiO_2,

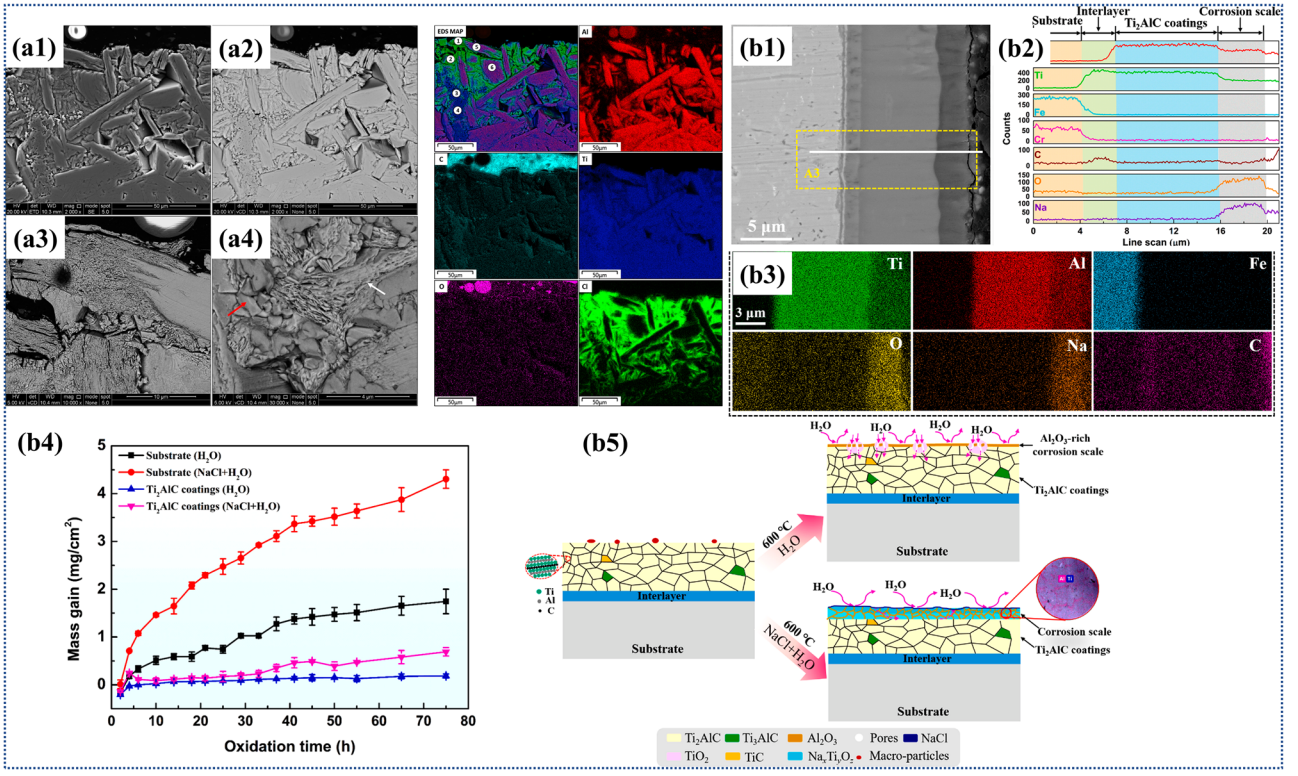


Figure 11. SEM cross-section morphologies of corroded Ti_3AlC_2 showing: (a1–a2) secondary electron and corresponding backscattered electron images of the reaction layer, (a3) backscattered image showing exfoliated Ti_3AlC_2 grain and (a4) backscattered image showing the corrosion product ($TiC_{0.67}$) in red arrow and exfoliated layer $Ti_3C_2Cl_2$ in white arrow. (reprinted with permission from [83]) (b1) Cross-sectional SEM micrographs of the corroded Ti_2AlC coatings at 600°C for 75 h in solid NaCl deposit in water vapor. (b2) The corresponding linescanning profiles of Al, Ti, Fe, Cr, C, O, Na elements along the white solid line in (b1). (b4) Mass gain versus exposure time for $1Cr_{11}Ni_2W_2MoV$ substrates and Ti_2AlC coatings exposed to H_2O and solid NaCl deposit in water vapor at 600°C. (b5) Schematic diagram of the corrosion mechanism for the Ti_2AlC coatings under water vapor and solid NaCl deposits in water vapor at 600°C for 75 h (reprinted with permission from [118]).

offering inadequate substrate protection during oxidation. However, in the marine environment, the corrosion results were opposite. Cr_2AlC showed poor heat corrosion resistance, reacting directly with NaCl to form the unprotected NaxAlyOz and Na_2CrO_4, while Ti_3SiC_2 exhibited the best corrosion resistance.

Wang et al. [118] investigated the synergistic corrosion properties of Ti_2AlC coating under solid NaCl deposition in 600°C water vapor for 75 h. A continuous corrosion scale was formed on the coating surface (Figure 11(b1)). This scale, primarily composed of Ti, Al, O, and Na elements (Figure 11(b2–b3)), showed a mass gain per unit area for Ti_2AlC coatings of $0.69 \pm 0.09\ mg/cm^2$, three times more than that in water vapor. (Figure 11(b4)). NaCl significantly accelerated the corrosion process of Ti_2AlC coatings at 600°C. Initially, Ti_2AlC corroded and oxidized to produce TiO_2 and Al_2O_3. However, the formed TiO_2 rapidly broke down due to chloride ions and water vapor invasion, generating a defective NaxTiyOz layer. Fortunately, Al_2O_3 amorphous phase filled the defects, modifying the corrosion scale structure to be more dense and less sensitive to Cl^- or H^+ ions. The schematic corrosion process is proposed in (Figure 11(b5)). For further study, the Al migration could be mitigated by synthesizing textured Ti_3AlC_2 with a base surface parallel to the surface, shielding Al layer consumption, or through appropriate pre-oxidation to form an alumina oxide skin resistant to chloride attack, enhancing the corrosion resistance and structural stability of the MAX phase.

5.2. Liquid lead-bismuth

Liquid lead and Lead-bismuth eutectic (LBE) are coolants for future accelerator-driven systems (ADS) and lead-cooled fast reactors (LFR), causing severe corrosion to structural materials at high temperatures. Developing new structural materials with superior corrosion resistance is essential to address the issue of lead-bismuth alloy corrosion. MAX phase materials, as radiation-resistant and high-temperature metal-ceramic structural materials, exhibit outstanding properties—high

temperature resistance, oxidation resistance, high strength, and corrosion resistance—making them crucial candidates for LFR structural materials [119–129].

In static LBE corrosion, two primary corrosion behaviors are observed: oxidation and dissolution. Oxidation corrosion involves a chemical process where elements in the material react with oxygen ions dissolved in LBE, forming corresponding oxides. The solution corrosion and permeation of structural materials by LBE are primarily influenced by the solubility of the materials in LBE and are related to the surface morphology. To enhance material corrosion resistance, controlling the oxygen concentration in LBE within an appropriate range is crucial, leading to the formation of a protective oxide layer on the surface.

Shi et al. [120] determined the corrosion resistance of MAX phase coatings to heavy liquid metals, ranking them as $Cr_2AlC > Ti_2AlC > Ti_3AlC_2 > V_2AlC$. The only Cr_2AlC forms the alumina-dominant layer, while others form an oxide mixture, either V-rich or titanium-rich, containing alumina. Ti_2AlC commonly includes the second phase of the Ti-Al alloy, TiC_2 or TiC_x, and the second phase of Ti_3AlC_2. Al, having the highest solubility in Pb compared to Ti and Si, preferentially dissolves, allowing LBE to permeate the material. Heinzel et al. [126] observed that the corrosion behavior of MAX in liquid LBE/Pb relied significantly on the second phase's behavior. The second phase, mainly Ti-Al compounds, was responsible for the poor performance of Ti_2AlC. The elevated activity of second phase Al led to rapid oxidation, emphasizing the need to avoid materials with high second-phase Al activity.

To identify the degradation resistant in oxygen-poor, fast-flowing liquid LBE, Lapauw et al. [125] assessed the intrinsic stability of 11 MAX-phase based materials in low-oxygen static LBE. A stronger interaction was observed in Ti_2SnC. As Sn melts at 232°C, the Sn-containing secondary phase in the material was removed and dissolved into the liquid LBE. For Ti_3AlC_2, intergranular LBE infiltration occurred in the Al-rich phase ($TiAl_3$), while the MAX phase grains remained unaffected. The distinction in liquid metal corrosion behavior between the MAX phase and its (often inevitable) parasitic phase further emphasized the need for high purity in MAX phase materials for HLM-cooled nuclear systems.

Charalampopoulou et al. [130] studied the protective role of the anticorrosion coating Cr_2AlC on DIN 1.4970 fuel cladding tubes through a 1000 h test in liquid LBE. The results demonstrated that the Cr_2AlC coating significantly mitigated dissolution corrosion. At the interface between Cr_2AlC and the steel substrate, the predominant structure comprised ultrafine, equiaxed Cr_2AlC grains with nickel diffused into them, forming in situ MAX phase solid solution. However, the authors did not conduct further TEM analysis on the as-deposited and exposed Cr_2AlC coatings.

Most MAX phases exhibit no interaction with LBE, except for Zr-rich MAX phases, which demonstrate localized interactions. [124] (Figure 12(a–e)). At first, Al outward diffusion from the Zr_2AlC MAX phase grains to GBs. Since Bi (143 pm) is smaller than Pb(154 pm), only Bi was found in partially affected Zr_2AlC grains. Then, Bi/Pb atoms penetrated the basal planes, potentially along stacking faults (SFs), or defect-rich areas in the MAX phase grains, to finally spread throughout the whole Zr_2AlC grains (Figure 12(f–g)). The Bi/Pb ingress into the Zr_2AlC grains, resulted in the in-situ formation of a new Zr_2(Al,Bi,Pb)C MAX phase solid solution (Figure 12(h–k)). The Zr_2AlC/LBE interaction mechanism was illustrated in (Figure 12(l)).

6. Ways to enhance the long-term protection

While the oxidation corrosion of MAX phases is extensively studied, the applications in higher temperature, longer time and more harsh chemical environment are increasingly urgent. Based on the physical and chemical characteristics and crystallographic configuration of the MAX phase, how to further improve its stability in harsh environments is particularly important. In the following sections, we summarized the general situation of oxidation induced self-healing, multi-elemental effects and machine learning based on current studies. It is hoped to further extend the service life of MAX phase and shorten the research cycles.

6.1. How to utilize and modify the crack healing behavior?

6.1.1. High oxygen partial pressure

The excellent high-temperature properties and autonomous crack healing abilities render MAX phase materials appealing for high-temperature applications [30,36,39–42,94,131–136].

Under high oxygen partial pressure, Li et al. [135] identified the main healing mechanism of Ti_2AlC, involving the filling of cracks with well-adhering α-Al_2O_3 grains and the presence of rutile TiO_2 (Figure 13 (a1–a3)). The healed samples exhibited a flexural strength that returned from its residual damaged strength value of 152–224 MPa, slightly surpassing the initial strength of 211 MPa (Figure 13(a4)).

The crack healing behavior of Cr_2AlC was also investigated by Pei et al. [40] using time-delayed X-ray computed tomography (CT) to monitor local crack-filling phenomena at 1200°C in air. They observed that the

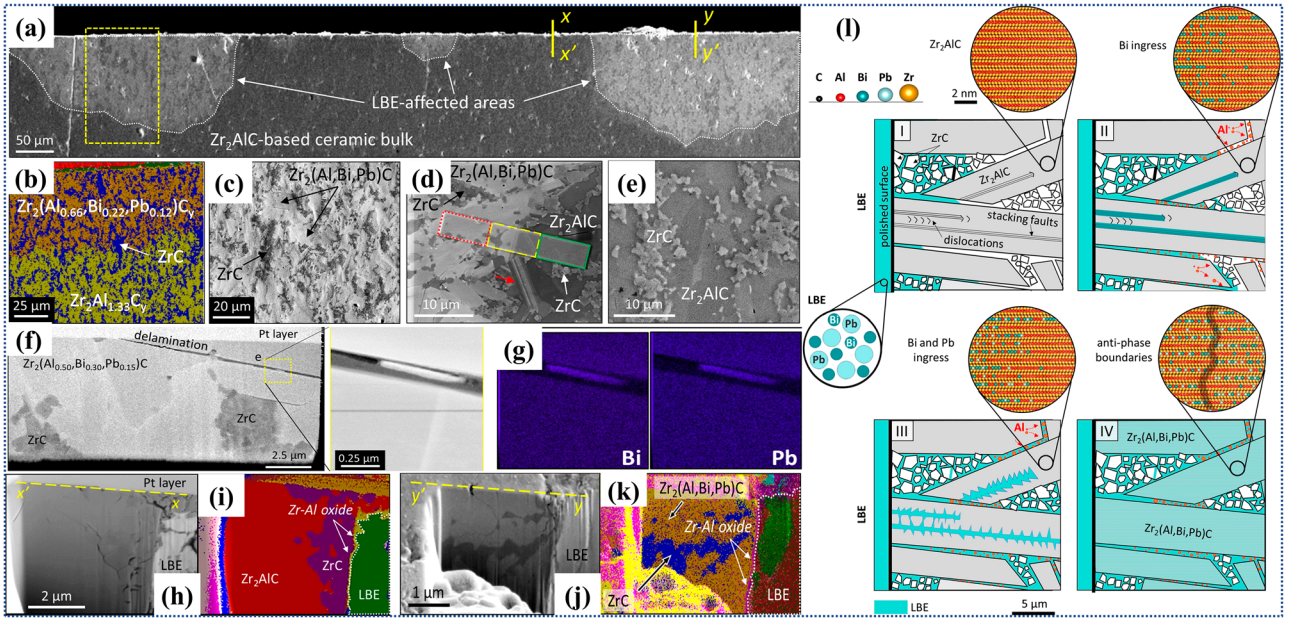


Figure 12. SEM images of the polished facet of the as-exposed Zr_2AlC ceramic: (a) overview showing local LBE interaction. (b) EDS phase map of the framed area in (a). Images of the Zr_2AlC/LBE interaction: (c) fully affected zone, (d) transition zone, and (e) unaffected sample bulk, (f) STEM image of a thin foil, showing a basal delamination in an LBE-affected Zr_2AlC MAX phase grain. (g) STEM-EDS elemental mapping of the area around the basal delamination, (h-k) SEM images of FIB cross-sectional trenches on the polished facet of LBE-exposed Zr_2AlC (l)Suggested Zr_2AlC/LBE interaction mechanism(reprinted with permission from [124]).

maximum crack could be fully healed by Al_2O_3 with a width of 4.8 µm for 4 h and 10 µm for 12 h, with the presence of Cr7C3 phase below the dense Al_2O_3 layer (Figure 13(b)). Due to the high oxidation temperature of Al, the oxidation-induced self-healing behavior requires elevated temperatures, generally exceeding 900°C [36,41,134]. Owing to the low cohesion energy and migration energy of Sn atoms, the movement and oxidation of Sn atoms at lower temperatures are promoted. Wang et al. [94] prepared a $Ti_2(Al_{0.6}Sn_{0.4})C$ solid solution coating using magnetron combination technology. The cracks caused by Vickers indentation on the coating's surface self-heal at 700°C, marking the lowest self-healing temperature observed in aluminum-based MAX phase coatings to date (Figure 13(c1–c6)). The formation of SnO_2 is a key factor in the crack self-healing of aluminum-based MAX phase coatings at low temperatures.

Self-healing involves three essential requirements: (i) flow into the crack, (ii) fill the crack volume, and (iii) adhere to the crack surface. For Mn + 1AXn phases, cracked surface oxidation provides sufficient volume expansion to fulfill the 'flow' criterion. Evaluating the high-temperature crack healing potential of MAX phase materials involves analyzing four main criteria: preferential oxidation of element A, rapid diffusion of element A, volume expansion upon oxidation, and adhesion of oxidation products. Additionally, mechanical assessment of the crack-filled oxide involves comparing its Young's modulus and coefficient of thermal expansion (CTE) with the parent MAX phase, considered as secondary standards. Effective crack healing occurred when the adhesion between the oxide filling the crack and the parent MAX phase was sufficient to restore its load-bearing capacity. This required the energy to separate the healing oxide from the MAX phase to be equal to or greater than the cohesion of the MAX phase. Prominent self-healing MAX phases include Ti_2AlC, Ti_3AlC_2, and Cr_2AlC, meeting both primary and secondary selection criteria. However, Cr_2AlC may induce compressive stress due to a larger CTE than the healing oxide. Other MAX phase compounds capable of selective oxidation-based crack healing at high temperatures include V_2AlC, V_3AlC_2, Nb_2AlC, Zr_2AlC, Zr_2AlN, and Ti_3SiC_2, among others. Adhesion energy between the healing oxide and adjacent MAX phases surpassed cohesion energy in all reviewed cases [41].

6.1.2. Low oxygen partial pressure

The above discussed oxidation-driven crack healing mechanism is effective in air. However, some high-temperature structural components, utilized in hypersonic vehicles during flight, gas turbines in combustion, and industrial vacuum furnaces during operation, are often exposed to low oxygen partial pressures.

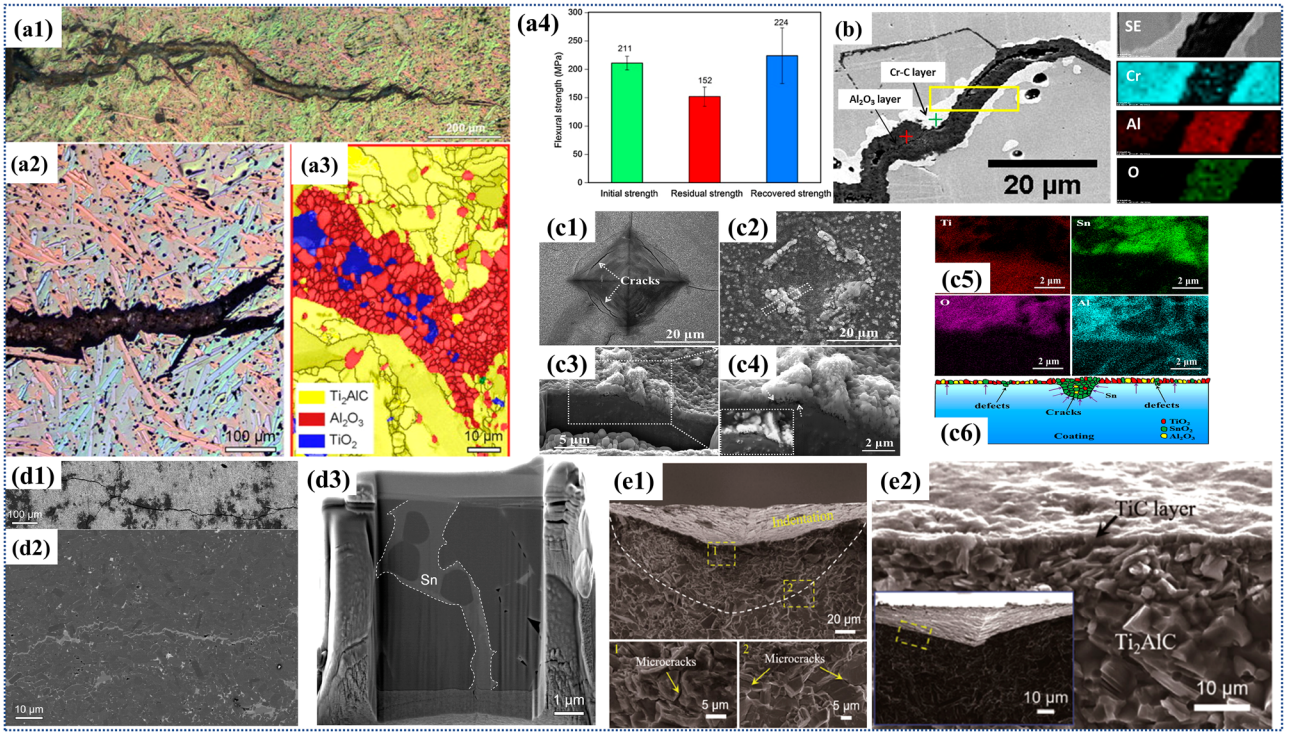


Figure 13. Low- and high-magnification images (a1) Optical overview image of the healed crack. (a2) An enlarged optical image taken from (a1).(a3)Two opposite fracture surfaces (a4)Flexural strength of the virginal Ti_2AlC, after creating crack damage and after crack healing(reprinted with permission from [135]) (b1)Secondary electron cross-sectional SEM image(reprinted with permission from [40]) (c1) the cracks on the surface of $Ti_2(Al0.6Sn0.4)C$ coating before self-healing. (c2) Microstructures of the surface cracks after self-healing. (c3) Low magnification image of the self-healing cracks after FIB milling. (c4) An enlarged image taken from the marked area in the set of (c3), the inset is the backscattered electron image. (c5) elements mapping: Ti, Sn, O, Al. (c6) Schematic illustration of $Ti_2(Al_{0.6}Sn_{0.4})C$ coating in self-healing. (reprinted with permission from [94]) (d1) SEM image of surface cracks (d2) Polished surfaces of Ti_2SnC after healing at 1000°C for 1 h (d3)Observation of the healed zones made by FIB. The healed zone is marked by dashed lines. (reprinted with permission from [137]) Cross-sectional SEM micrographs: (e1) damaged Ti_2AlC sample; and Ti_2AlC samples after healing for 2 h at (e2) 1200°C (reprinted with permission from [131]).

For MAX phases, elements with low melting points, such as Al, Ga, Sn, In, and Pb, can easily diffuse from the cell structure of MAX at high temperatures. Li et al. [137] investigated crack healing of Ti_2SnC ceramic in a vacuum. The results revealed that the crack was filled only with metallic Sn at temperatures above 800°C for just 1 h in a vacuum (Figure 13(d1–d3)). Additionally, the high mobility of Sn may facilitate the redistribution of residual stresses in the healed crack zones generated due to thermal expansion mismatch upon cooling. Researchers discovered that decomposition-induced crack healing is another mechanism for Ti_2AlC at temperatures above 1200°C and low oxygen partial pressure. This mechanism may be effective in Al or Si-containing MAX phases (Ti_2AlC, Cr_2AlC, Ti_3AlC_2, and Ti_3SiC_2), initiated by the decomposition of MAX on the surface into carbides (such as TiC_x or $Cr_{23}C_6$) at high temperatures. For instance, the self-healing behavior of Ti_2AlC at a low oxygen partial pressure of about 1 Pa was studied [131]. The results indicated that Ti_2AlC decomposition to TiC_x can repair the damage (Figure 13(e1–e2)). The volume shrinkage caused by the decomposition of Ti_2AlC creates compressive stress in the TiC_x layer. Additionally, after cooling from the healing temperature, the thermal expansion mismatch between the TiC_x layer and the Ti_2AlC matrix also causes compressive stress on the healing surface. The thermal expansion coefficients of Ti_2AlC and TiC_x are 8.8×10^{-6} and $(7.4–8.3) \times 10^{-6}$ K^{-1}, respectively. The compressive stress generated in the TiC_x layer acts as surface prestressing to counteract the tensile stress applied to the surface of the Ti_2AlC material.

The mechanism of crack self-healing in MAX phases varies between air and low-oxygen environments. In air, high temperatures induce the formation of Al_2O_3, which fills the cracks. In low-oxygen environments, elements with low melting points from the A site migrate to and fill the cracks. Additionally, at high temperatures, the decomposition of the MAX phase forms MX carbides, generating compressive stress within the cracks, which promotes healing.

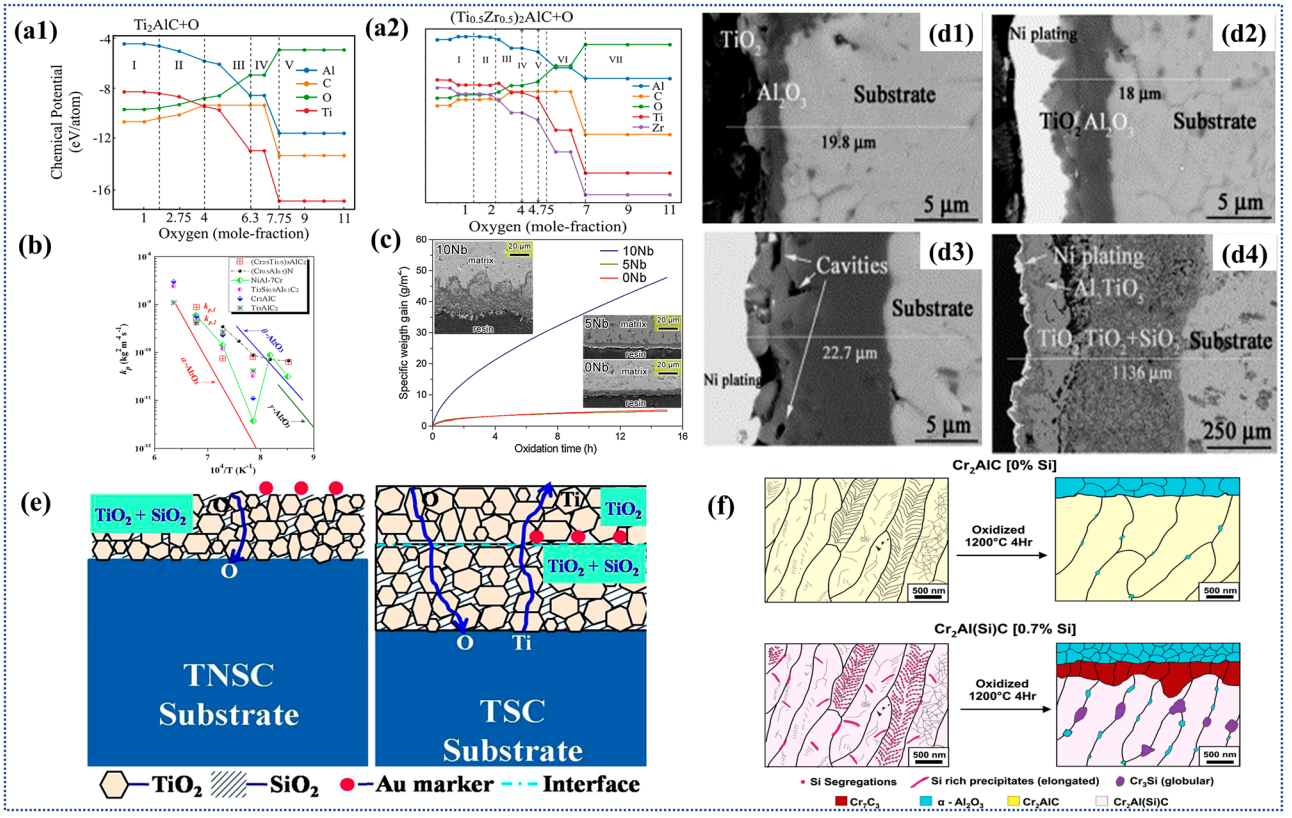


Figure 14. Change in elemental chemical activity of elements during oxidation of (a1) Ti_2AlC, and (a2) $(Ti_{0.5}Zr_{0.5})_2AlC$ at 1500 K as a function of molar oxygen (reprinted with permission from [11]). (b) Temperature dependences of kp values of the as-prepared $(Cr_{2/3}Ti_{1/3})_3AlC_2$ sample, Cr_2AlC, Ti_3AlC_2, NiAl-7Cr, $(Cr_{0.5}Al_{0.5})N$, $Ti_3Si_{0.9}Al_{0.1}C_2$(reprinted with permission from [139]). (c)Specific weight gains against oxidation time at 1200°C. The insets are SEM morphologies of the oxide scale (reprinted with permission from [95]). Back-scattered electron images of cross-sections of $Ti_3Si_{0.9}Al_{0.1}C_2$ oxidized at: (d1) 1100°C, (d2) 1200°C, (d3) 1300°C, and (d4) 1350°C (reprinted with permission from [96]). (e) Schematic diagram of the oxidation mechanism of (a) Nb doped and (b) Nb free Ti_3SiC_2(reprinted with permission from [143]). (f) Schematic representations of oxidation-induced changes in the morphology of the Cr_2AlC and $Cr_2Al(Si)C$ coatings(reprinted with permission from [140]).

6.2. How to understand the muti-elemental effect?

In recent years, high entropy alloys have gained attention for their superior mechanical properties and significantly improved oxidation resistance. MAX phases can also form solid solutions at various positions, including M-site, A-site, and X-site solid solutions. Recently, researchers have discovered that desired performance can be achieved by adding elements especially in M or A positions. Studies revealed that chemical disorder were modified by adjusting elements, which can impact the oxidation behavior of MAX phases. [11,45,49,94,138–141].

6.2.1. M-site modification

P. Singh et al. [11] observed an increase in chemical activity of Al with rising oxygen content (Figure 14(a1)), directly influencing the formation of a protective oxide layer. However, Zr doping notably alters Al's chemical activity in Ti_2AlC, slowing the rate of protective Al_2O_3 formation (Figure 14(a2)).

Compared to Cr_2AlC, the oxidation behavior of Ti-doped $(Cr_{2/3}Ti_{1/3})_3AlC_2$ underwent a different transformation [139]. The temperature dependences of kp values of the as prepared $(Cr_{2/3}Ti_{1/3})_3AlC_2$ was shown in Figure 14(b). Initially, a TiO_2 layer formed on the surface. The presence of doped would become the Ti ion transport, leading to the formation of a non-protective oxide layer on the surface. The primary products of these oxide layers include Cr_2O_3, $(Cr,Al)_2O_3$, and rutile TiO_2, with Cr_2TiO_5 and $(Cr_{0.222}Ti_{0.778})O_{1.889}$. In addition, the Ti-doped Nb_4AlC_3 was also investigated by Gu et al [142]. Compared to Nb_4AlC_3, the $(Nb_{1-x}Ti_x)_4AlC_3$ solid solution exhibited significantly enhanced oxidation resistance. This is primarily attributed to the formation of a more protective oxide layer composed of $TiNb_2O_7$ and $NbAlO_4$.

Zhang et al. [95] studied Nb doping's impact on the structural stability and oxidation resistance of $(Ti_{1-x}Nb_x)_3AlC_2$. Uniform distribution of Nb dopant within polycrystalline grains, occupying Ti sites at an

atomic level, was observed. Structural stability remained until x = 0.15, beyond which the Nb-doped '312' phase decomposed.

A dense continuous Al_2O_3 protective layer was established on both pristine and 5% Nb-doped Ti_3AlC_2. $(Ti_{0.95}Nb_{0.05})_3AlC_2$ exhibits almost identical oxidation resistance to Ti_3AlC_2. However, for $(Ti_{0.9}Nb_{0.1})_3AlC_2$, the oxide film composed of Al_2O_3, TiO_2, and Nb_2O_5 is curved and porous, resulting in inferior protective properties. (Figure 14(c)).

To explore the impact of Nb doping on oxidation mechanism of $(Ti,Nb)_3SiC_2$, Zheng et al. [143]. investigated ionic transport behavior and growth mechanisms of oxide scales on Nb-doped and undoped Ti_3SiC_2 at 800°C in air. Results revealed enhanced oxidation resistance in Ti_3SiC_2 due to Nb doping. Post-doping, oxidation of $(Ti,Nb)_3SiC_2$ was solely controlled by inward O diffusion, while outward Ti diffusion was completely restrained. The oxide layer transitioned from a duplex-layer of TiO_2 outer and $TiO_2 + SiO_2$ inner layers to a single $TiO_2 + SiO_2$ mixture layer. Defect chemistry theory analysis suggested Nb doping reduced concentrations of oxygen vacancies and Ti interstitials in formed TiO_2, restraining outward Ti diffusion and reducing oxidation rates. The Schematic diagram of the oxidation mechanism of Nb doped and Nb free Ti_3SiC_2 was shown in Figure 14(e).

Yu et al. [138] investigated the oxidation behavior of $(Ti,Nb,Ta)_4AlC_3$ containing Cr-Al phase. The results showed that highly porous $(Ti,Nb,Ta)O_4$ would be formed on its surface at first. With the increase of temperature, the liquid phase of Cr-Al would diffuse into $(Ti,Nb,Ta)O_4$. And oxidation to form a dense and continuous Al_2O_3 layer, improve the oxidation resistance of MAX phase.

6.2.2. A-site modification

To enhance the oxidation resistance of MAX phases, incorporating antioxidative elements in the A-site solid solution proves effective. Commonly solid-solved elements in the A-site include Al, Si, Sn, and others. Zhang et al. [96] conducted a study by introducing Al into Ti_3SiC_2, forming $Ti_3Si_{0.9}Al_{0.1}C_2$ solid solution, and investigated its behavior at temperatures ranging from 1000 to 1350°C in air. In comparison to Ti_3SiC_2, $Ti_3Si_{0.9}Al_{0.1}C_2$ demonstrated significantly improved oxidation resistance at 1000–1300°C, attributed to the formation of a continuous α-Al_2O_3 layer. Within this temperature range, the parabolic rate constants of $Ti_3Si_{0.9}Al_{0.1}C_2$ decreased by 2–4 orders of magnitude. At 1000–1100°C, the oxide layer exhibited a continuous α-Al_2O_3 inner layer and a discontinuous TiO_2 (rutile) outer layer (Figure 14(d1)). At 1200–1300°C, the oxidation layer comprised a continuous α-Al_2O_3 inner layer and discontinuous TiO_2 (rutile) and Al_2TiO_5 outer layers (Figure 14(d2–d3)). At 1350°C, the continuous α-Al_2O_3 layer could not be maintained due to a vigorous reaction between Al_2O_3 and TiO_2 (Figure 14(d4)). The formation of a continuous α-Al_2O_3 layer is attributed to two key factors: the high activity and diffusion of Al and the low oxygen solubility within the solid solution.

Shang et al. [63] investigated the effect of Si additions on the oxidation behavior of Cr_2AlC-based coatings. The presence of Si in Cr_2AlC inhibited grain growth during oxidation. Additionally, after oxidation, MAX phase samples containing 0.7 at% Si showed a significant increase in the number of oxide grains per unit of interface length at the oxide/coating interface compared to MAX phase samples without Si addition. The presence of silicon increases the nucleation density of Al_2O_3 grains in the oxide. The thickness of Al_2O_3 induced by Si concentration increased by 40%.

Pradeep et al. [140] investigated the impact of Si addition on Cr_2AlC phase oxidation. Results indicated that during high-temperature oxidation, Cr_3Si phase precipitated at the grain boundary of MAX phase, playing a crucial role at the interface. Compared with MAX without Si addition, grain coarsening decreased, hindering grain growth. Schematic representations of oxidation-induced changes in the morphology of Cr_2AlC and $Cr_2Al(Si)C$ coatings were shown in (Figure 14(f)). Kashkarov et al. [144] investigated the oxidation resistance of $Ti_3Al(Si)C_2$ and Ti_3SiC_2-based composites. Results revealed that the formation of Al-rich $Ti_3Al(Si)C_2$ phase in the outer layer improves the corrosion resistance of Ti_3SiC_2 matrix composites at 1300°C. The high corrosion resistance of MAX phase is linked to the growth of a continuous Al_2O_3 oxide layer. Due to the growth of R-$TiO_2 + Al_2TiO_5$/R-$TiO_2 + SiO_2$ porous oxide layer, the corrosion resistance of Ti_3SiC_2-based composites is poor at 1300°C. Shang et al. [63] investigated the effect of Si additions on the oxidation behavior of Cr_2AlC-based coatings. The presence of Si in Cr_2AlC inhibited grain growth during oxidation. Additionally, after oxidation, MAX phase samples containing 0.7 at% Si showed a significant increase in the number of oxide grains per unit of interface length at the oxide/coating interface compared to MAX phase samples without Si addition. The presence of silicon increases the nucleation density of Al_2O_3 grains in the oxide. The thickness of Al_2O_3 induced by Si concentration increased by 40%.

Drouelle et al. [17] demonstrated that substituting Al atoms with Sn atoms in the A plane of the MAX phase harms oxidation resistance. Guo et al. [45] revealed through first-principles calculations that Sn doping weakens the Ti-Al bond, reducing the oxidation

resistance of Ti_3AlC_2 powder. Tin doping typically accelerates the oxidation process of Ti_3AlC_2 powder. Consequently, the oxidation product (anatase TiO_2) and $Ti_3Al_{0.8}Sn_{0.2}C_2$ powder develop more cracks and flanges at the low-temperature stage due to different thermal expansion coefficients, creating a rapid oxygen diffusion channel that intensifies oxidation. Sn doping lowers the initial temperature of anatase TiO_2 to rutile TiO_2 by 50°C and the reaction fraction of $Ti_3Al_{0.8}Sn_{0.2}C_2$ powder at 600°C. At the high-temperature stage, Sn doping promotes the formation and growth of rutile TiO_2, expediting oxidation.

Modification of the M and A elements in MAX phases can regulate oxidation resistance. Through element doping, the activity of oxide-forming elements like Al can be adjusted to control the growth of Al_2O_3. This can also lead to the formation of protective oxides such as $TiNb_2O_7$ and $NbAlO_4$. Furthermore, element doping can hinder the diffusion of Ti at the M-site, reducing the formation of the detrimental oxide TiO_2, altering the structure of the mixed oxide layer, and improving oxidation resistance. However, some dopants can negatively affect oxidation resistance. For instance, Sn doping increases residual stress in the oxide layer, compromising its integrity, and promotes the formation of TiO_2, thus reducing the oxidation resistance of the MAX phase.

6.3. Machine learning

At high temperatures, MAX phases exhibit complex oxidation and competitive growth behavior among oxidation products. Interpreting oxidation laws faces two major challenges: acquiring comprehensive oxidation data and establishing reliable kinetic models. Machine learning (ML) offers a precise approach to address the long-term complex oxidation of various MAX phases. Traditionally, isothermal oxidation, including thermogravimetric (TG) experiments, occurred at fixed intervals, often overlooking crucial transition phase information. The MAX phases oxidation behavior is influenced by factors like temperature, oxygen partial pressure, stress, sample density, and shape. Traditional orthogonal experiments considering multiple variables demand more time and cost. Machine learning (ML), including deep learning (DL), efficiently handles complex tasks and has become an invaluable tool in materials science (Figure 15).

A trained ML/DL model can comprehend and predict trends in data changes across various factors, acquiring data much faster than experimental and numerical methods. This greatly expedites material design, performance evaluation, and optimization. [145–148]. In addition, Singh P et al. [11]. investigated the oxidation mechanism of the $(Ti_{0.5}Zr_{0.5})_2AlC$ MAX phase using a high-throughput machine learning framework. The results showed that Zr has a strong effect on the disordering of the M site (at Ti) of Ti_2AlC, and Zr doping significantly changed the chemical activity of Ti_2AlC by slowing down the chemical activity of Al under high oxygen exposure. Sauceda et al. [33] developed a machine learn-driven high-throughput framework for rapid assessment of the phase stability and oxygen reactivity of the 211 chemical MAX phase M_2AX. The results revealed that the predicted results were consistent with the experimental results of Ti_2AlC oxidation. In addition, it demonstrated that the stability of Ti_2SiC competing phase was high, so it cannot be synthesized by experiment.

7. Summary and Recommendations

7.1. Summary

The preparation and formation mechanisms of MAX phases in various forms were summarized in this work, proposing a relatively unified formation pathway and discussing synthesis temperatures, purity concerns, different elements, bonding, and various morphologies of MAX phases. The primary factors influencing the oxidation of MAX phases and their corrosion mechanisms were discussed in various environments like air, water, salt solutions, Pb-Bi, etc. Finally, the future development direction like machine learning and high entropy MAX phase was proposed.

1. For the synthesis of MAX bulks, initial reactions lead to the formation of MX phases and MA compounds (such as Ti-Al, Cr-Al, etc.). Subsequently, the MX phase dissolves into the liquid phase MA compound, giving rise to the MAX phase. Synthesis with pure elementals often leads to the formation of various impurity phases due to slow element diffusion, impacting purity and raising concerns about Al element volatilization. The use of intermediate MX as a starting material significantly reduces the reaction barrier for MAX phase formation, prevents the generation of impurity phases and lowers the synthesis temperature. For the formation of MAX films, the precise control of element thickness can significantly reduce the synthesis temperature. Direct deposition of intermediate MX can effectively regulate the diffusion path of elements and improve the purity.

2. The oxidation process of MAX phases induces the diffusion of active elements (usually on A site) and the formation of oxide layer. Beneath the oxidation layer, new phases are formed due to the composition changes induced by element diffusion. Since there are many elements that can form oxides in MAX, layered oxides or

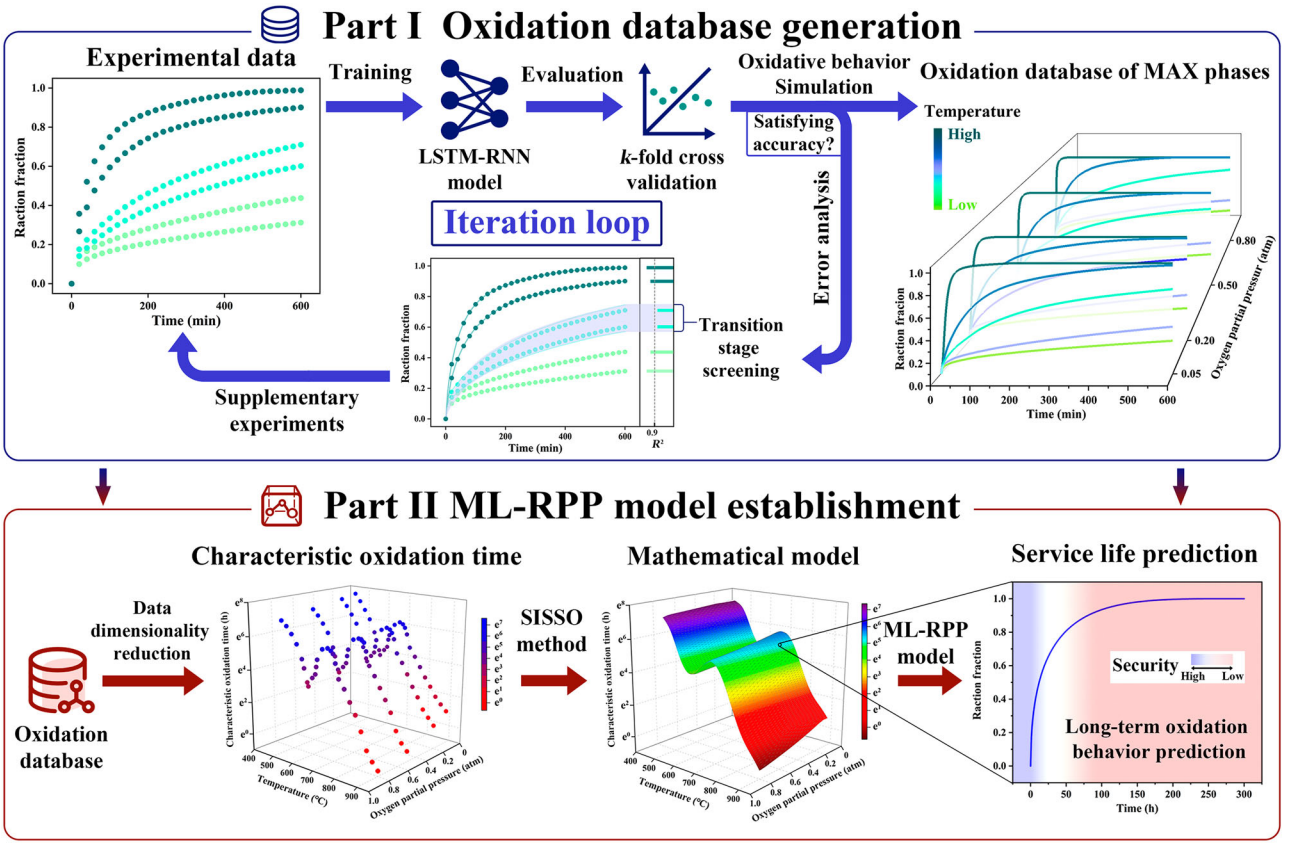


Figure 15. Flowchart of the method of oxidation database generation and oxidation kinetic model establishment of MAX phases(reprinted with permission from [145]).

composite oxides can be formed under the synergistic influence of thermodynamics and dynamics. For the MAX system that can form multi-oxides, it is very likely to face problems such as irregular oxidation products and excessive internal stress. How to regulate the matrix phase change before and after the diffusion of these active elements, as well as the coordination of multilayer or composite oxidation structure is very important.

3. Compared to air exposure, MAX phases exhibit an accelerated oxidation rate in water environments. The ionization of H_2O into hydroxide ions has an enhanced diffusion rate, generating gaseous compounds along with H_2. This disrupts the structural integrity of the oxide layer. In high-temperature high-pressure water environments, the degradation of aluminum oxide and silicon oxide further diminishes the protective efficacy of MAX phases. In salt solution environments, alkali metal ions interact with Al_2O_3, forming various sodium salts. These salts, when the temperature exceeds 800°C, volatilize and decompose, compromising the structural density of the oxide layer and reducing the corrosion resistance of MAX phases. In Pb-Bi environments with low oxygen content, the initial occupation of smaller-radius Pb/Bi atoms along grain boundaries and defect regions inhibits the formation of a protective oxide film on the surface.

4. Regulating grain size and modifying grain boundaries enable control over the diffusion pathways of active atoms and the rapid formation of protective oxide films. In addition, the unique crystal structure of MAX phase results in different diffusion rates of elements on different crystal planes. The diffusion behavior of active elements can be affected by the adjustment of crystal planes in MAX. Surface roughness also plays a pivotal role in the oxidation of MAX phases. Rough surfaces induce residual stresses within oxides, leading to crack formation and diminishing the antioxidation capability of MAX phases. The A-position elements that are essential for MAX phase self- healing include Al, Sn, Si, etc. Under typical atmospheric conditions, the increased temperature leads to the formation of oxides through the oxidation of the A-site atoms, which fill the cracks with oxides and achieve repair. In low oxygen environment, MAX phase is decomposed into MX carbide, which is conducive to crack closure.

7.2. Recommendations

1. In situ techniques for understanding the oxidation behavior**:** Employing in situ techniques such as high-temperature X-ray diffraction (XRD) and

transmission electron microscopy (TEM) to study the real-time oxidation behavior of MAX phases under operational conditions.

2. Nano-structuring for enhancing the oxidation resistance: Utilizing nanotechnology to create MAX phase coatings with improved adherence and reduced oxidation rates through grain boundary engineering and surface modification.
3. Doping for enhancing oxidation resistance: Doping M-site and A-site elements has the potential to reduce defects in the oxidation layer, increasing its density and thereby improving the oxidation resistance of MAX phases. Future research might explore optimal element selection and doping strategies customized for complex corrosive environments.
4. Lowering self-repair temperatures and improving oxidation resistance: MAX phases typically require high temperatures for self-repair, but A-site doping with Sn can lower these temperatures. The challenge ahead is to find methods for achieving self-repair at lower temperatures without compromising MAX phases' oxidation resistance.
5. Developing an oxidation kinetics model: The oxidation of MAX phases involves multiple factors, making the process complex and far-reaching. Utilizing machine learning to collect comprehensive oxidation data and build an oxidation kinetics model would significantly assist in accurately predicting and addressing oxidation issues in MAX phases.

Credit authorship contribution statement

Min Guo: Investigation, Writing—original draft, Writing—review & editing. **Guoqin Cao:** Methodology, Writing—review & editing. **Haoyu Pan:** Investigation. **Junhong Guo:** Investigation and Analysis. **Chaoyang Chen:** Investigation. **Baofeng Zhang:** Investigation. **Junhua Hu:** Supervision, Conceptualization, Visualization, Funding acquisition.

Disclosure statement

No potential conflict of interest was reported by the author(s).

Funding

This work was supported by Education Department of Henan Province [grant number 23A430014]; National Natural Science Foundation of China [grant number 52171082]; Natural Science Foundation Project for Outstanding Youth of Henan Province [grant number 232300421013]; Nuclear Material Technology Innovation Fund for National Defense Technology Industry [grant number ICNM-2023-YZ-02]; LONGMEN laboratory [grant number LMOYTSKT009]; Science and Technology Department of Henan Province [grant number 232102230043, 232102241036, 2323004210413].

Data availability statement

No data was used for the research described in the article.

ORCID

Junhua Hu http://orcid.org/0000-0003-0191-1503

References

[1] Gonzalez-Julian J. Processing of MAX phases: from synthesis to applications. J Am Ceram Soc. 2020;104:659–690. doi: 10.1111/jace.17544

[2] Lin ZJ, Li MS, Wang JY, et al. High-temperature oxidation and hot corrosion of Cr_2AlC. Acta Mater. 2007;55:6182–6191. doi:10.1016/j.actamat.2007.07.024

[3] Eklund P, Beckers M, Jansson U, et al. The $M_{n+1}AX_n$ phases: materials science and thin-film processing. Thin Solid Films. 2010;518:1851–1878. doi:10.1016/j.tsf.2009.07.184

[4] Eklund P, Rosen J, Persson POÅ. Layered ternary $M_{n+1}AX_n$ phases and their 2D derivative MXene: an overview from a thin-film perspective. J Phys D: Appl Phys. 2017;50:113001. doi:10.1088/1361-6463/aa57bc

[5] Sun ZM, Hashimoto H, Zhang ZF, et al. Synthesis and characterization of a metallic ceramic material–Ti_3SiC_2. Mater Trans 2006;47:170–174. doi:10.2320/matertrans.47.170

[6] Radovic M, Barsoum MWJACSB. MAX phases: bridging the gap between metals and ceramics. Am Ceram Soc Bull. 2013;92:20–27.

[7] Magnuson M, Mattesini M. Chemical bonding and electronic-structure in MAX phases as viewed by X-ray spectroscopy and density functional theory. Thin Solid Films. 2017;621:108–130. doi:10.1016/j.tsf.2016.11.005

[8] Zheng L, Wang J, Lu X, et al. $(Ti_{0.5}Nb_{0.5})_5AlC_4$: a new-layered compound belonging to MAX phases. J Am Ceram Soc. 2010;93:3068–3071. doi:10.1111/j.1551-2916.2010.04056.x

[9] Lin Z, Zhuo M, Zhou Y, et al. Microstructures and theoretical bulk modulus of layered ternary tantalum aluminum carbides. J Am Ceram Soc. 2006;89:3765–3769. doi:10.1111/j.1551-2916.2006.01303.x

[10] Zhang J, Liu B, Wang J, et al. Low-temperature instability of Ti_2SnC: a combined transmission electron microscopy, differential scanning calorimetry, and X-ray diffraction investigations. J Mater Res. 2009;24:39–49. doi:10.1557/JMR.2009.0012

[11] Singh P, Sauceda D, Arroyave R. High temperature oxidation behavior of disordered $(Ti_{0.5}Zr_{0.5})_2AlC$ MAX phase via a Machine Learning-Augmented DFT approach. Mater Lett X. 2021;10:100062. doi: 10.1016/j.mlblux.2021.100062

[12] Cao Y, Guo C, Wu D, et al. Synthesis and corrosion resistance of solid solution $Ti_3(Al_{1-x}Si_x)C_2$. J Alloys Compd. 2021;867:159126. doi:10.1016/j.jallcom.2021.159126

[13] Cabioc'h T, Eklund P, Mauchamp V, et al. Structural investigation of substoichiometry and solid solution effects in $Ti_2Al(C_x,N_{1-x})_y$ compounds. J Eur Ceram

Soc. 2012;32:1803–1811. doi:10.1016/j.jeurceramsoc.2011.12.011
[14] Scabarozi TH, Hettinger JD, Lofland SE, et al. Epitaxial growth and electrical-transport properties of $Ti_7Si_2C_5$ thin films synthesized by reactive sputter-deposition. Scr Mater. 2011;65:811–814. doi:10.1016/j.scriptamat.2011.07.038
[15] Lane NJ, Naguib M, Lu J, et al. Structure of a new bulk $Ti_5Al_2C_3$ MAX phase produced by the topotactic transformation of Ti_2AlC. J Eur Ceram Soc. 2012;32:3485–3491. doi:10.1016/j.jeurceramsoc.2012.03.035
[16] Rao JC, Pei YT, Yang HJ, et al. TEM study of the initial oxide scales of Ti_2AlC. Acta Mater. 2011;59:5216–5223. doi:10.1016/j.actamat.2011.04.058
[17] Drouelle E, Brunet V, Cormier J, et al. Oxidation resistance of Ti_3AlC_2 and $Ti_3Al_{0.8}Sn_{0.2}C_2$ MAX phases: A comparison. J Am Ceram Soc. 2020;103:1270–1280. doi:10.1111/jace.16780
[18] Atazadeh N, Heydari S, Baharvandi M, et al. Reviewing the effects of different additives on the synthesis of the Ti_3SiC_2 MAX phase by mechanical alloying technique. Int J Refract Met Hard Mater. 2016;61:67–78. doi:10.1016/j.ijrmhm.2016.08.003
[19] Aleksanyan AG, Dolukhanyan SK, Mayilyan DG, et al. Formation of Ti_2AlN_x MAX phase by "Hydride Cycle" and SHS methods. Ceram Int. 2023;49:24229–24234. doi:10.1016/j.ceramint.2022.11.350
[20] Torres C, Quispe R, Calderón NZ, et al. Development of the phase composition and the properties of Ti_2AlC and Ti_3AlC_2 MAX-phase thin films – a multilayer approach towards high phase purity. Appl Surf Sci. 2021;537:147864. doi:10.1016/j.apsusc.2020.147864
[21] Nickl JJ, Schweitzer KK, Luxenberg P. Gasphasenabscheidung im system Ti-Si-C. J Less Common Metals. 1972;26:335–353. doi:10.1016/0022-5088(72)90083-5
[22] Barsoum MW. The $M_{N+1}AX_N$ phases: a new class of solids: Thermodynamically stable nanolaminates. Prog Solid State Chem. 2000;28:201–281. doi:10.1016/S0079-6786(00)00006-6
[23] Ching WY, Mo Y, Aryal S, et al. Intrinsic mechanical properties of 20 MAX-phase compounds. J Am Ceram Soc. 2013;96:2292–2297. doi:10.1111/jace.12376
[24] Barsoum MW, Radovic M. Elastic and mechanical properties of the MAX phases. Annu Rev Mater Res. 2011;41:195–227. doi:10.1146/annurev-matsci-062910-100448
[25] Yu T, Chen H, Hu T, et al. Recent advances in the applications of encapsulated transition-metal nanoparticles in advanced oxidation processes for degradation of organic pollutants: a critical review. Appl Catal B-Environ. 2024;342:123401. doi:10.1016/j.apcatb.2023.123401
[26] Sokol M, Natu V, Kota S, et al. Big questions in chemistry – on the chemical diversity of the MAX phases. Trends Chem. 2019;1:210–223. doi:10.1016/j.trechm.2019.02.016
[27] Sun ZM. Progress in research and development on MAX phases: a family of layered ternary compounds. Int Mater Rev. 2011;56:143–166. doi:10.1179/1743280410Y.0000000001
[28] Barsoum M W, Tzenov N, Procopio A, et al. Oxidation of $Ti_{n+1}AlX_n$ (n = 1 3 and X = C, N): II. Experimental Results. J Electrochem Soc. 2001;148:C551. doi:10.1149/1.1380256
[29] Palmquist JP, Jansson U, Seppänen T, et al. Magnetron sputtered epitaxial single-phase Ti_3SiC_2 thin films. Appl Phys Lett. 2002;81:835–837. doi:10.1063/1.1494865
[30] Song GM, Pei YT, Sloof WG, et al. Oxidation-induced crack healing in Ti_3AlC_2 ceramics. Scr Mater. 2008;58:13–16. doi:10.1016/j.scriptamat.2007.09.006
[31] Naguib M, Kurtoglu M, Presser V, et al. Two-dimensional nanocrystals produced by exfoliation of Ti_3AlC_2. Adv Mater. 2011;23:4248–4253. doi:10.1002/adma.201102306
[32] Fashandi H, Dahlqvist M, Lu J, et al. Synthesis of Ti_3AuC_2, $Ti_3Au_2C_2$ and Ti_3IrC_2 by noble metal substitution reaction in Ti_3SiC_2 for high-temperature-stable Ohmic contacts to SiC. Nat Mater. 2017;16:814–818. doi:10.1038/nmat4896
[33] Sauceda D, Singh P, Falkowski AR, et al. High-throughput reaction engineering to assess the oxidation stability of MAX phases. Npj Comput Mater. 2021;7:6. doi:10.1038/s41524-020-00464-7
[34] Badie S, Sebold D, Vaßen R, et al. Mechanism for breakaway oxidation of the Ti_2AlC MAX phase. Acta Mater. 2021;215:117025. doi:10.1016/j.actamat.2021.117025
[35] Bao W, Wang X-G, Ding H, et al. High-entropy M_2AlC-MC (M = Ti, Zr, Hf, Nb. Ta) composite: synthesis and microstructures. Scr Mater. 2020;183:33–38. doi:10.1016/j.scriptamat.2020.03.015
[36] Yang HJ, Pei YT, De Hosson JTM. Oxide-scale growth on Cr_2AlC ceramic and its consequence for self-healing. Scr Mater. 2013;69:203–206. doi:10.1016/j.scriptamat.2013.04.013
[37] Cui B, Jayaseelan DD, Lee WE. Microstructural evolution during high-temperature oxidation of Ti_2AlC ceramics. Acta Mater. 2011;59:4116–4125. doi:10.1016/j.actamat.2011.03.035
[38] Qian XK, He XD, Li YB, et al. Cyclic oxidation of Ti_3AlC_2 at 1000–1300 °C in air. Corros Sci. 2011;53:290–295. doi:10.1016/j.corsci.2010.09.033
[39] Boatemaa L, Bosch M, Farle AS, et al. Autonomous high-temperature healing of surface cracks in Al_2O_3 containing Ti_2AlC particles. J Am Ceram Soc. 2018;101:5684–5693. doi:10.1111/jace.15793
[40] Pei R, McDonald SA, Shen L, et al. Crack healing behaviour of Cr_2AlC MAX phase studied by X-ray tomography. J Eur Ceram Soc. 2017;37:441–450. doi:10.1016/j.jeurceramsoc.2016.07.018
[41] Farle A-S, Kwakernaak C, van der Zwaag S, et al. A conceptual study into the potential of $M_{n+1}AXn$-phase ceramics for self-healing of crack damage. J Eur Ceram Soc. 2015;35:37–45. doi:10.1016/j.jeurceramsoc.2014.08.046
[42] Yang HJ, Pei YT, Song GM, et al. Healing performance of Ti_2AlC ceramic studied with in situ microcantilever bending. J Eur Ceram Soc. 2013;33:383–391. doi:10.1016/j.jeurceramsoc.2012.09.012
[43] Azina C, Mráz S, Greczynski G, et al. Oxidation behaviour of V_2AlC MAX phase coatings. J Eur Ceram

Soc. 2020;40:4436–4444. doi:10.1016/j.jeurceramsoc.2020.05.080
[44] Wang Z, Ma G, Liu L, et al. High-performance Cr_2AlC MAX phase coatings: oxidation mechanisms in the 900–1100 °C temperature range. Corros Sci. 2020;167:108492. doi:10.1016/j.corsci.2020.108492
[45] Guo C, Wang E, Wang S, et al. Oxidation mechanism of MAX phases (Ti_3AlC_2 powders) with and without Sn doping. Corros Sci. 2021;180:109197. doi:10.1016/j.corsci.2020.109197
[46] Smialek JL. Oxidation of Al_2O_3 scale-forming MAX phases in turbine environments. Metall Mater Trans A. 2018;49:782–792. doi:10.1007/s11661-017-4346-9
[47] Zhang Z, Lai DMY, Lim SH, et al. Isothermal oxidation of the Ti_2AlC MAX phase coatings deposited by kerosene-fuelled HVOF spray. Corros Sci. 2018;138:266–274. doi:10.1016/j.corsci.2018.04.022
[48] Maier BR, Garcia-Diaz BL, Hauch B, et al. Cold spray deposition of Ti_2AlC coatings for improved nuclear fuel cladding. J Nucl Mater. 2015;466:712–717. doi:10.1016/j.jnucmat.2015.06.028
[49] Azina C, Tunca B, Petruhins A, et al. Deposition of MAX phase-containing thin films from a $(Ti,Zr)_2AlC$ compound target. Appl Surf Sci. 2021;551:149370. doi:10.1016/j.apsusc.2021.149370
[50] Wang Z, Li W, Liu Y, et al. Diffusion-controlled intercalation approach to synthesize the Ti_2AlC MAX phase coatings at low temperature of 550 °C. Appl Surf Sci. 2020;502:144130. doi:10.1016/j.apsusc.2019.144130
[51] Tian Y, Xiao H, Ren L, et al. A new strategy to fabricate Ti_2AlC MAX coatings by the two-step laser method. Surf Coat Technol. 2022;448:128944. doi:10.1016/j.surfcoat.2022.128944
[52] Zhang F, Yan S, Li C, et al. Synthesis and characterization of MAX phase Cr_2AlC based composite coatings by plasma spraying and post annealing. J Eur Ceram Soc. 2019;39:5132–5139. doi:10.1016/j.jeurceramsoc.2019.08.039
[53] Mane RB, Haribabu A, Panigrahi BB. Synthesis and sintering of Ti_3GeC_2 MAX phase powders. Ceram Int. 2018;44:890–893. doi:10.1016/j.ceramint.2017.10.017
[54] Atazadeh N, Saeedi Heydari M, Baharvandi HR, et al. Reviewing the effects of different additives on the synthesis of the Ti_3SiC_2 MAX phase by mechanical alloying technique. Int J Refract Met H. 2016;61:67–78. doi:10.1016/j.ijrmhm.2016.08.003
[55] Pazniak A, Bazhin P, Shplis N, et al. Ti3C2Tx MXene characterization produced from SHS-ground Ti_3AlC_2. Mater Des. 2019;183:108143. doi:10.1016/j.matdes.2019.108143
[56] Etebarian S, Sarpoolaky H, Rezaie HR, et al. Synthesis of Ti_3SiC_2 MAX phase powder through molten salt method. Int J Appl Ceram Technol. 2023;20:2166–2174. doi:10.1111/ijac.14358
[57] Su K, Tian X, Li Z, et al. Oxidation behavior of Ti_3SiC_2 powder synthesized by using biochar, Si and Ti. Ceram Int. 2022;19:4863–4871. doi: 10.1016/j.ceramint.2022.09.377
[58] Galyshev SN, Bazhin PM, Stolin AM, et al. High-temperature firing of composite based on the max-phase of the Ti–Al–C system. Refract Ind Ceram. 2018;58:557–561. doi:10.1007/s11148-018-0144-1
[59] Berastegui P, Riekehr L, Jansson U. Magnetron sputtering of nanolaminated Cr_2AlB_2. Coatings. 2020;10:735. doi:10.3390/coatings10080735
[60] Tang C, Steinbrück M, Klimenkov M, et al. Textured growth of polycrystalline MAX phase carbide coatings via thermal annealing of M/C/Al multilayers. J Vac Sci Technol A. 2020;38:013401. doi:10.1116/1.5131544
[61] Tang C, Klimenkov M, Jaentsch U, et al. Synthesis and characterization of Ti_2AlC coatings by magnetron sputtering from three elemental targets and ex-situ annealing. Surf Coat Technol. 2017;309:445–455. doi:10.1016/j.surfcoat.2016.11.090
[62] Zhang Z, Qian Y, Xu J, et al. Effect of annealing on microstructure evolution and corrosion resistance of an amorphous Cr-Al-C coating. Corros Sci. 2021;178:109062. doi:10.1016/j.corsci.2020.109062
[63] Shang L, Konda Gokuldoss P, Sandlöbes S, et al. Effect of Si additions on the Al_2O_3 grain refinement upon oxidation of Cr_2AlC MAX phase. J Eur Ceram Soc. 2017;37:1339–1347. doi:10.1016/j.jeurceramsoc.2016.11.050
[64] Tang C, Steinbrück M, Grosse M, et al. The effect of annealing temperature on the microstructure and properties of Cr–C–Al coatings on zircaloy-4 for accident-tolerant fuel (ATF) applications. Coatings. 2022;12:167. doi:10.3390/coatings12020167
[65] Abdulkadhim A, Takahashi T, Music D, et al. MAX phase formation by intercalation upon annealing of TiC /Al ($0.4 \leq x \leq 1$) bilayer thin films. Acta Mater. 2011;59:6168–6175. doi:10.1016/j.actamat.2011.06.029
[66] Liu E, Hu T, Al-Dhabi NA, et al. MOF-derived Fe/Ni@C marigold-like nanosheets as heterogeneous electro-Fenton cathode for efficient antibiotic oxytetracycline degradation. Environ Res. 2024;247:118357. doi:10.1016/j.envres.2024.118357
[67] Su C, Soyol-Erdene T-O, Bayanjargal O, et al. Facile synthesis of coral-like nitrogen and sulfur co-doped carbon-encapsulated FeS_2 for efficient electroreduction of nitrate to ammonia. Sep Purif Technol. 2024;348:127813. doi:10.1016/j.seppur.2024.127813
[68] Xing W, Luo K, Liang J, et al. Urchin-like core–shell tungsten oxide@ carbon composite electrode for highly efficient and stable water desalination via hybrid capacitive deionization (HCDI). Chem Eng J. 2023;477:147268. doi:10.1016/j.cej.2023.147268
[69] Zhang H, Gao Y, Meng S, et al. Metal sulfide S-Scheme homojunction for photocatalytic selective phenylcarbinol oxidation. Adv Sci. 2024;11:2400099. doi:10.1002/advs.202400099
[70] Meng S, Chen C, Gu X, et al. Efficient photocatalytic H_2 evolution, CO_2 reduction and N_2 fixation coupled with organic synthesis by cocatalyst and vacancies engineering. Appl Catal B-Environ. 2021;285:119789. doi:10.1016/j.apcatb.2020.119789
[71] Yuan J, Wang Z, Ma G, et al. MAX phase forming mechanism of M–Al–C (M = Ti, V, Cr) coatings: in-situ X-ray diffraction and first-principle calculations. Mater Sci Technol. 2023;143:140–152. doi:10.1016/j.jmst.2022.09.045

[72] Zhang Y, Luo F, Bai Q, et al. In-situ X-ray diffraction study on dealloying: a scenario of a $Cu_{90}Au_{10}$ alloy. J Phys Chem Solids. 2021;150:109879. doi:10.1016/j.jpcs.2020.109879
[73] Alami J, Eklund P, Emmerlich J, et al. High-power impulse magnetron sputtering of Ti–Si–C thin films from a Ti_3SiC_2 compound target. Thin Solid Films. 2006;515:1731–1736. doi:10.1016/j.tsf.2006.06.015
[74] Li Z, Zhou G, Wang Z, et al. HiPIMS induced high-purity Ti_3AlC_2 MAX phase coating at low-temperature of 700 °C. J Eur Ceram Soc. 2023;43:4673–4683. doi:10.1016/j.jeurceramsoc.2023.03.059
[75] Wang XH, Zhou YC. Microstructure and properties of Ti_3AlC_2 prepared by the solid–liquid reaction synthesis and simultaneous in-situ hot pressing process. Acta Mater. 2002;50:3141–3151. doi: 10.1016/S1359-6454(02)00117-9
[76] Pampuch R, Lis J, Stobierski L, et al. Solid combustion synthesis of Ti_3SiC_2. J Eur Ceram Soc. 1989;5:283–287. doi:10.1016/0955-2219(89)90022-8
[77] Lis J, Miyamoto Y, Pampuch R, et al. Ti_3SiC-based materials prepared by HIP-SHS techniques. Mater Lett. 1995;22:163–168. doi:10.1016/0167-577X(94)00246-0
[78] Magnus C, Cooper D, Sharp J, et al. Microstructural evolution and wear mechanism of Ti_3AlC_2 –Ti_2AlC dual MAX phase composite consolidated by spark plasma sintering (SPS). Wear. 2019;438:203013. doi:10.1016/j.wear.2019.203013
[79] Akhlaghi M, Tayebifard SA, Salahi E, et al. Self-propagating high-temperature synthesis of Ti_3AlC_2 MAX phase from mechanically-activated Ti/Al/graphite powder mixture. Ceram Int. 2018;44:9671–9678. doi:10.1016/j.ceramint.2018.02.195
[80] Qiao L, Bi J, Liang G, et al. Synthesis and electromagnetic wave absorption performances of a novel $(Mo_{0.25}Cr_{0.25}Ti_{0.25}V_{0.25})_3AlC_2$ high-entropy MAX phase. Mater Sci Technol. 2023;137:112–122. doi:10.1016/j.jmst.2022.07.039
[81] Zhao S, Chen L, Xiao H, et al. Phase transformation and amorphization resistance in high-entropy MAX phase M_2SnC (M = Ti, V, Nb, Zr, Hf) under in-situ ion irradiation. Acta Mater. 2022;238:118222. doi:10.1016/j.actamat.2022.118222
[82] Ghosh NC, Harimkar SP. Consolidation and synthesis of MAX phases by Spark Plasma Sintering (SPS): a review. Adv Sci Technol $M_{n+1}AXn$ Phases. 2012: 47–80. doi:10.1533/9780857096012.47
[83] Magnus C, Cooper D, Jantzen C, et al. Synthesis and high temperature corrosion behaviour of nearly monolithic Ti_3AlC_2 MAX phase in molten chloride salt. Corros Sci. 2021;182:109193. doi:10.1016/j.corsci.2020.109193
[84] Yunus M, Kumar R, Maji BC, et al. An optimized method for synthesizing phase-pure Ti_3AlC_2 MAX-phase through spark plasma sintering. J Eur Ceram Soc. 2022;42:354–363. doi:10.1016/j.jeurceramsoc.2021.10.030
[85] Ma XL, Zhu YL, Wang XH, et al. Microstructural characterization of bulk Ti_3AlC_2ceramics. Philos Mag. 2004;84:2969–2977. doi:10.1080/14786430410001716197
[86] Meng F, Liang B, Wang M. Investigation of formation mechanism of Ti_3SiC_2 by self-propagating high-temperature synthesis. Int J Refract Met H. 2013;41:152–161. doi:10.1016/j.ijrmhm.2013.03.005
[87] Han J-H, Hwang S-S, Lee D, et al. Synthesis and mechanical properties of Ti_3AlC_2 by hot pressing TiCx/Al powder mixture. J Eur Ceram Soc. 2008;28:979–988. doi:10.1016/j.jeurceramsoc.2007.09.015
[88] Zuber A, Gauthier-Brunet V, Roger J, et al. Cr_2AlC high temperature oxidation under dry and wet air: Understanding of the oxidation mechanism. J Eur Ceram Soc. 2023;43:5159–5167. doi:10.1016/j.jeurceramsoc.2023.05.012
[89] Ougier M, Michau A, Lomello F, et al. High-temperature oxidation behavior of HiPIMS as-deposited Cr–Al–C and annealed Cr_2AlC coatings on Zr-based alloy. J Nucl Mater. 2020;528:151855. doi:10.1016/j.jnucmat.2019.151855
[90] Li W, Wang Z, Shuai J, et al. A high oxidation resistance Ti_2AlC coating on Zirlo substrates for loss-of-coolant accident conditions. Ceram Int. 2019;45:13912–13922. doi:10.1016/j.ceramint.2019.04.089
[91] Gonzalez-Julian J, Onrubia S, Bram M, et al. High-temperature oxidation and compressive strength of Cr_2AlC MAX phase foams with controlled porosity. J Am Ceram Soc. 2018;101:542–552. doi:10.1111/jace.15224
[92] Smialek JL, Harder BJ, Garg A. Oxidative durability of TBCs on Ti_2AlC MAX phase substrates. Surf Coat Technol. 2016;285:77–86. doi:10.1016/j.surfcoat.2015.11.018
[93] Basu S, Obando N, Gowdy A, et al. Long-term oxidation of Ti_2AlC in air and water vapor at 1000–1300 °C temperature range. J Electrochem Soc. 2011;159:C90–C96. doi:10.1149/2.052202jes
[94] Wang Z, Sun J, Xu B, et al. Reducing the self-healing temperature of Ti_2AlC MAX phase coating by substituting Al with Sn. J Eur Ceram Soc. 2020;40:197–201. doi:10.1016/j.jeurceramsoc.2019.09.009
[95] Zhang H, Li Z, Zhang C, et al. Nb doping in Ti_3AlC_2: effects on phase stability, high-temperature compressive properties, and oxidation resistance. J Eur Ceram Soc. 2017;37:3641–3645. doi:10.1016/j.jeurceramsoc.2017.04.026
[96] Zhang HB, Zhou YC, Bao YW, et al. Improving the oxidation resistance of Ti_3SiC_2 by forming a $Ti_3Si_{0.9}A_{l0.1}C_2$ solid solution. Acta Mater. 2004;52:3631–3637. doi:10.1016/j.actamat.2004.04.015
[97] Hajas DE, to Baben M, Hallstedt B, et al. Oxidation of Cr_2AlC coatings in the temperature range of 1230 to 1410 °C. Surf Coat Technol. 2011;206:591–598. doi:10.1016/j.surfcoat.2011.03.086
[98] Sun Z, Zhou Y, Li M. Oxidation behaviour of Ti_3SiC_2-based ceramic at 900–1300 °C in air. Corros Sci. 2001;43:1095–1109. doi:10.1016/S0010-938X(00)00142-6
[99] Zuber A, Gauthier-Brunet V, Roger J, et al. Towards a better understanding of the high-temperature oxidation of MAX phase Cr_2AlC. J Eur Ceram Soc. 2022;42:2089–2096. doi:10.1016/j.jeurceramsoc.2021.12.057
[100] Yu W, Vallet M, Levraut B, et al. Oxidation mechanisms in bulk Ti_2AlC: influence of the grain size. J Eur Ceram

Soc. 2020;40:1820–1828. doi:10.1016/j.jeurceramsoc.2020.01.042
[101] Drouelle E, Gauthier-Brunet V, Cormier J, et al. Microstructure-oxidation resistance relationship in Ti_3AlC_2 MAX phase. J Alloys Compd. 2020;826:154062. doi:10.1016/j.jallcom.2020.154062
[102] Zhang J, Wang JY, Zhou YC. Structure stability of Ti_3AlC_2 in Cu and microstructure evolution of Cu–Ti_3AlC_2 composites. Acta Mater. 2007;55:4381–4390. doi:10.1016/j.actamat.2007.03.033
[103] Xu L, Zhu D, Liu Y, et al. Effect of texture on oxidation resistance of Ti_3AlC_2. J Eur Ceram Soc. 2018;38:3417–3423. doi:10.1016/j.jeurceramsoc.2018.03.009
[104] Chen X, Stelzer B, Hans M, et al. Enhancing the high temperature oxidation behavior of Cr_2AlC coatings by reducing grain boundary nanoporosity. Mater Res Lett. 2020;9:127–133. doi:10.1080/21663831.2020.1854358
[105] Badie S, Dash A, Sohn YJ, et al. Synthesis, sintering, and effect of surface roughness on oxidation of submicron Ti2AlC ceramics. J Am Ceram Soc. 2020;104:1669–1688. doi:10.1111/jace.17582
[106] Zhu W, Li X, Zheng C, et al. Hydrothermal corrosion behavior of Ti_3SiC_2 MAX phase at atomic scale under simulated PWR conditions. Corros Sci. 2022;209:110728. doi:10.1016/j.corsci.2022.110728
[107] Tang C, Große M, Ulrich S, et al. High-temperature oxidation and hydrothermal corrosion of textured Cr_2AlC-based coatings on zirconium alloy fuel cladding. Surf Coat Technol. 2021;419:127263. doi:10.1016/j.surfcoat.2021.127263
[108] Wang Z, Li X, Li W, et al. Comparative study on oxidation behavior of Ti_2AlN coatings in air and pure steam. Ceram Int. 2019;45:9260–9270. doi:10.1016/j.ceramint.2019.02.004
[109] Ward J, Bowden D, Prestat E, et al. Corrosion performance of Ti_3SiC_2, Ti_3AlC_2, Ti_2AlC and Cr_2AlC MAX phases in simulated primary water conditions. Corros Sci. 2018;139:444–453. doi:10.1016/j.corsci.2018.04.034
[110] Tang C, Steinbrueck M, Stueber M, et al. Deposition, characterization and high-temperature steam oxidation behavior of single-phase Ti_2AlC-coated Zircaloy-4. Corros Sci. 2018;135:87–98. doi:10.1016/j.corsci.2018.02.035
[111] Tang C, Steinbrück M, Große M, et al. Oxidation behavior of Ti_2AlC in the temperature range of 1400 °C – 1600 °C in steam. J Nucl Mater. 2017;490:130–142. doi:10.1016/j.jnucmat.2017.03.016
[112] Smialek JL. Environmental resistance of a Ti_2AlC-type MAX phase in a high pressure burner rig. J Eur Ceram Soc. 2017;37:23–34. doi:10.1016/j.jeurceramsoc.2016.07.038
[113] Du Y, Liu J-X, Gu Y, et al. Anisotropic corrosion of Ti_2AlC and Ti_3AlC_2 in supercritical water at 500°C. Ceram Int. 2017;43:7166–7171. doi:10.1016/j.ceramint.2017.02.153
[114] Feng Z, Ke P, Huang Q, et al. The scaling behavior and mechanism of Ti_2AlC MAX phase coatings in air and pure water vapor. Surf Coat Technol. 2015;272:380–386. doi:10.1016/j.surfcoat.2015.03.037
[115] Zhang H, Presser V, Berthold C, et al. Mechanisms and kinetics of the hydrothermal oxidation of bulk titanium silicon carbide. J Am Ceram Soc. 2010;93:1148–1155. doi:10.1111/j.1551-2916.2009.03570.x
[116] Lin ZJ, Li MS, Wang JY, et al. Influence of water vapor on the oxidation behavior of Ti_3AlC_2 and Ti_2AlC. Scr Mater. 2008;58:29–32. doi:10.1016/j.scriptamat.2007.09.011
[117] Li X, Wang S, Wu G, et al. Oxidation and hot corrosion behaviors of MAX-phase Ti_3SiC_2, Ti_2AlC, Cr_2AlC. Ceram Int. 2022;48:26618–26628. doi:10.1016/j.ceramint.2022.05.356
[118] Wang Z, Ma G, Li Z, et al. Corrosion mechanism of Ti_2AlC MAX phase coatings under the synergistic effects of water vapor and solid NaCl at 600 °C. Corros Sci. 2021;192:109788. doi:10.1016/j.corsci.2021.109788
[119] Heinzel A, Müller G, Weisenburger A. Compatibility of Ti_3SiC_2 with liquid Pb and PbBi containing oxygen. J Nucl Mater. 2009;392:255–258. doi:10.1016/j.jnucmat.2009.03.004
[120] Shi H, Azmi R, Han L, et al. Corrosion behavior of Al-containing MAX-phase coatings exposed to oxygen containing molten Pb at 600 °C. Corros Sci. 2022;201:110275. doi:10.1016/j.corsci.2022.110275
[121] Serag E, Caers B, Schuurmans P, et al. Challenges and coating solutions for wear and corrosion inside Lead Bismuth Eutectic: a review. Surf Coat Technol. 2022;441:128542. doi:10.1016/j.surfcoat.2022.128542
[122] Lyu L, Qiu X, Yue H, et al. Corrosion behavior of Ti_3SiC_2 in flowing liquid lead-bismuth eutectic at 500 °C. Materials (Basel). 2022;15:7406. doi:10.3390/ma15217406
[123] Zhu H, Liu X, Chang B, et al. Corrosion properties of Ti_3SiC_2 and Ti_3AlC_2 in static liquid lead–bismuth eutectic at 500 °C. Mater Corros. 2021;73:196–206. doi:10.1002/maco.202112586
[124] Tunca B, Lapauw T, Callaert C, et al. Compatibility of Zr_2AlC MAX phase-based ceramics with oxygen-poor, static liquid lead–bismuth eutectic. Corros Sci. 2020;171:108704. doi:10.1016/j.corsci.2020.108704
[125] Lapauw T, Tunca B, Joris J, et al. Interaction of $M_{n+1}AX_n$ phases with oxygen-poor, static and fast-flowing liquid lead-bismuth eutectic. J Nucl Mater. 2019;520:258–272. doi:10.1016/j.jnucmat.2019.04.010
[126] Heinzel A, Weisenburger A, Müller G. Long-term corrosion tests of Ti_3SiC_2 and Ti_2AlC in oxygen containing LBE at temperatures up to 700 °C. J Nucl Mater. 2016;482:114–123. doi:10.1016/j.jnucmat.2016.10.007
[127] Ghidiu M, Bentzel GW, Griggs J, et al. On the interactions of Ti_2AlC, Ti_3AlC_2, Ti_3SiC_2 and Cr_2AlC with pure sodium at 550 °C and 750 °C. Corros Sci. 2016;111:568–573. doi:10.1016/j.corsci.2016.05.045
[128] Zhang J, Li N. Review of the studies on fundamental issues in LBE corrosion. J Nucl Mater. 2008;373:351–377. doi:10.1016/j.jnucmat.2007.06.019
[129] Barnes LA, Dietz Rago NL, Leibowitz L. Corrosion of ternary carbides by molten lead. J Nucl Mater. 2008;373:424–428. doi:10.1016/j.jnucmat.2007.04.054
[130] Charalampopoulou E, Lambrinou K, Van der Donck T, et al. Early stages of dissolution corrosion in 316L and DIN 1.4970 austenitic stainless steels with and

without anticorrosion coatings in static liquid lead-bismuth eutectic (LBE) at 500 °C. Mater Charact. 2021;178:111234. doi:10.1016/j.matchar.2021.111234
[131] Yao B, Li S, Zhang W, et al. Self-healing behavior of Ti_2AlC at a low oxygen partial pressure. J Adv Ceram. 2022;11:1687–1695. doi:10.1007/s40145-022-0640-0
[132] Bei GP, Pedimonte BJ, Pezoldt M, et al. Crack healing in $Ti_2Al_{0.5}Sn_{0.5}C$-Al_2O_3 composites. J Am Ceram Soc. 2015;98:1604–1610. doi:10.1111/jace.13496
[133] Li S, Xiao L, Song G, et al. Oxidation and crack healing behavior of a fine-grained Cr_2AlC ceramic. J Am Ceram Soc. 2013;96:892–899. doi:10.1111/jace.12170
[134] Yang HJ, Pei YT, Rao JC, et al. Self-healing performance of Ti_2AlC ceramic. J Mater Chem. 2012;22:8304–8313. doi:10.1039/c2jm16123k
[135] Li S, Song G, Kwakernaak K, et al. Multiple crack healing of a Ti_2AlC ceramic. J Eur Ceram Soc. 2012;32:1813–1820. doi:10.1016/j.jeurceramsoc.2012.01.017
[136] Yang HJ, Pei YT, Rao JC, et al. High temperature healing of Ti2AlC: on the origin of inhomogeneous oxide scale. Scr Mater. 2011;65:135–138. doi:10.1016/j.scriptamat.2011.03.031
[137] Li S, Zhang L, Yu W, et al. Precipitation induced crack healing in a Ti_2SnC ceramic in vacuum. Ceram Int. 2017;43:6963–6966. doi:10.1016/j.ceramint.2017.02.120
[138] Yu D, Tan Y. Oxidation behaviors of compositionally complex MAX phases in air. Ceram Int. 2021;47:30188–30193. doi:10.1016/j.ceramint.2021.07.198
[139] Liu Z, Yang J, Qian Y, et al. High temperature oxidation behavior of quaternary ordered $(Cr_{2/3}Ti_{1/3})_3AlC_2$-based MAX ceramic. Corros Sci. 2021;183:109317. doi:10.1016/j.corsci.2021.109317
[140] Pradeep KG, Chang K, Kovács A, et al. Nano-scale Si segregation and precipitation in $Cr_2Al(Si)C$ MAX phase coatings impeding grain growth during oxidation. Mater Res Lett. 2019;7:180–187. doi:10.1080/21663831.2019.1572663
[141] Greczynski G, Hultman L, Odén M. X-ray photoelectron spectroscopy studies of Ti_1-AlN ($0 \leq x \leq 0.83$) high-temperature oxidation: the crucial role of Al concentration. Surf Coat Technol. 2019;374:923–934. doi:10.1016/j.surfcoat.2019.06.081
[142] Gu J, Pan L, Yang J, et al. Mechanical properties and oxidation behavior of Ti-doped Nb_4AlC_3. J Eur Ceram Soc. 2016;36:1001–1008. doi:10.1016/j.jeurceramsoc.2015.10.023
[143] Zheng L, Hua Q, Li X, et al. Investigation on the effect of Nb doping on the oxidation mechanism of Ti_3SiC_2. Corros Sci. 2018;140:374–378. doi:10.1016/j.corsci.2018.05.028
[144] Kashkarov EB, Krotkevich DG, Mingazova YR, et al. Functionally graded laminated composites fabricated from MAX-phase filled preceramic papers: microstructure, mechanical properties and oxidation resistance. J Eur Ceram Soc. 2022;42:2062–2072. doi:10.1016/j.jeurceramsoc.2022.01.023
[145] Guo C, Duan X, Fang Z, et al. A new strategy for long-term complex oxidation of MAX phases: database generation and oxidation kinetic model establishment with aid of machine learning. Acta Mater. 2022;241:118378. doi:10.1016/j.actamat.2022.118378
[146] Zhao Z, Bieler TR, Llorca J, et al. Grain boundary slip transfer classification and metric selection with artificial neural networks. Scr Mater. 2020;185:71–75. doi:10.1016/j.scriptamat.2020.04.029
[147] Dai W, Wang H, Guan Q, et al. Studying the micromechanical behaviors of a polycrystalline metal by artificial neural networks. Acta Mater. 2021;214:117006. doi:10.1016/j.actamat.2021.117006
[148] Zhou X-Y, Zhu J-H, Wu Y, et al. Machine learning assisted design of FeCoNiCrMn high-entropy alloys with ultra-low hydrogen diffusion coefficients. Acta Mater 2022;224:117535. doi:10.1016/j.actamat.2021.117535